ARTICLE

https://doi.org/10.1590/2317-4889202120210011

BJGEO
Brazilian Journal of Geology

Melt-melt immiscibility and implications for the origin of Madeira albite-rich granite, Pitinga mine, Amazonas, Brazil: A melt inclusion study

Régis Munhoz Krás Borges[1]*, Lucas Eustáquio Dias Amorim[2], Francisco Javier Rios[2], Gabrielle Cristine Silva dos Santos[1], Monica Elizetti Freitas[2], Tatiana Aparecida Fernandes de Lima[2], Armindo Santos[2], Tércio Assunção Pedrosa[2]

Abstract

Presented here are the results of the first studies of silicate melt inclusions hosted in quartz crystals from the two late granitic facies of the Paleoproterozoic Madeira pluton in the Pitinga mine, State of Amazonas, Brazil. The study of these magmatic inclusions in the anorogenic granites of Pitinga furnished reliable results because the original composition of the trapped silicate liquids is well preserved. Petrographic, morphological, and chemical data show that both porphyritic hypersolvus alkali feldspar granite and albite-rich granite were formed by melt-melt immiscibility from a precursor magma. After phase separation, albite-rich granite evolution was characterized by strong enrichment in F, Na, Sn, Nb, Ta, Zr, Th, Y, Rb, and REE compared to the porphyritic granite, based on data obtained from analyses of both trace elements by laser ablation inductively coupled plasma mass spectrometry (LA-ICP-MS) and major elements by electron microprobe. These elements make up the polymetallic magmatic ore of the Pitinga mine. The contrasting evolutionary trends, peralkaline and peraluminous, stand out in the different geochemical signatures of the analyzed melt inclusions. The preliminary results of our studies on melt inclusions trapped in rare metal granite minerals from Sn-polymetallic deposits in Brazil suggest abundant possibilities for using this methodology in future petrological and metallogenic research.

KEYWORDS: melt inclusions; melt-melt immiscibility; LA-ICP-MS; electron microprobe; peralkaline albite-rich granite; Pitinga mine.

INTRODUCTION

Silicate melt inclusions are small quantities of silicate melt that are trapped in minerals during their growth or crystallization, and, as such, can provide information about the physical parameters and chemical compositions of the magmatic environment (Sorby 1858, Roedder 1979, 1984b, Lowenstern 1995, Frezzotti 2001).

These inclusions are protected from any processes or reactions that may occur in an evolving magma-fluid environment (cooling, crystallization, decompression, degassing, contamination), recording information on a particular evolution stage of a magmatic system (Kamenetsky and Kamenetsky 2010, Amorim *et al.* 2012). Thus, these entrapped inclusions in early crystallized phases allow primary magmas to be characterized, while revealing their subsequent chemical evolution in more differentiated rocks (Frezzotti 2001). In addition, melt inclusions have been increasingly studied to understand the role of magmatic processes in the formation of ore deposits (Bodnar and Student 2006).

Melt inclusions, or magmatic inclusions (Roedder 1979), are present in volcanic and plutonic rocks, being more common in the former, and reach up to a few tens of micrometers. In volcanic rocks, they are generally large (> 50 µm), glassy, and are hosted in transparent minerals. However, in plutonic rocks, they are usually crystallized and appear as small opaque (< 20 µm) or granular textured spots. When observed at higher magnification, they appear as dark masses with poorly defined contact with their host.

The study of silicate melt inclusions in minerals of granitic and pegmatitic rocks has been used by several authors, for example, in Bolivia porphyry systems (Dietrich *et al.* 2000); in Cu-Mo-rich porphyry systems from Chile (Davidson and Kamenetsky 2001); in Variscan S-type granites from Ehrenfriedersdorf and Eibenstock in central parts of Erzgebirge, Germany (Thomas *et al.* 2006); and in granites and pegmatites and their genetic relationships (Thomas *et al.* 2012, Thomas and Davidson 2013).

In addition, there is a higher number of studies about liquid-liquid or liquid-fluid immiscibility (Veksler 2004, Kamenetsky 2006, Thomas *et al.* 2006, Kamenetsky and Kamenetsky 2010), addressing both petrogenetic aspects and those involving the exsolution of mineralizing fluids.

[1]Instituto de Geociências, Universidade Federal do Pará – Belém (PA), Brazil. E-mails: munhoz@ufpa.br, santos.gabrielle2011@gmail.com

[2]Laboratório de Caracterização Mineralógica e Metalogênese, Centro de Desenvolvimento da Tecnologia Nuclear, Comissão Nacional de Energia Nuclear – Belo Horizonte (MG), Brazil. E-mails: ledamorim@cdtn.br, javier@cdtn.br, monicaef@gmail.com, tatiaflima@gmail.com, santosa@cdtn.br, tap@cdtn.br

*Corresponding author.

The study of silicate melts is generally carried out in rocks of the post-Mesozoic age and, especially, in more recent rocks where inclusions are preserved and have no signs of recrystallization. However, studies on Proterozoic rocks are rare, mainly because the melts appear fully recrystallized.

In Brazil, Proterozoic magmatic rocks commonly show features of deformation produced by tectonic events that occurred after emplacement, notably the Brasiliano cycle. Such events can delete the records of these silicate melts. In this sense, the alkaline granites of the Pitinga Province are considered a unique opportunity to study melt inclusions because they were not subjected to deformational events after being positioned in the crust.

The Pitinga mine region comprises two highly fractionated A-type granite plutons with ages Pb-Pb in zircon of 1.82 Ga (Costi *et al.* 2000), called Madeira (Costi 2000, Minuzzi 2005) and Água Boa (Lenharo *et al.* 2002, 2003). Together with the Europa pluton, they form the Madeira Suite (Costi 2000). The magmatic ore is composed of cassiterite, cryolite, pyrochlore, columbite, and zircon, associated with the albite-rich granite facies of the Madeira pluton (Costi *et al.* 2005, Costi *et al.* 2009, Bastos Neto *et al.* 2005, Bastos Neto *et al.* 2009).

The albite-rich granite is composed of two facies, a dominant magmatic core facies and a metasomatic border facies, situated along the top and border zones of the albite-rich granite. The core facies is peralkaline and cryolite-bearing, and the border albite-rich granite facies is peraluminous to metaluminous, oxidized, and fluorite-bearing. The albite-rich granite and porphyritic hypersolvus alkali feldspar granite display contact relationships, both in outcrops and in the drill core, indicating that both facies were comagmatic and coeval (Costi 2000, Costi *et al.* 2009). These authors suggested that the albite-rich granite resulted from a phase separation process, similar to the one recorded by Thomas *et al.* (2006) in the Variscan Erzgebirge granites. The peralkaline phase had separated from a parental melt, most probably slightly peralkaline to metaluminous, with a composition similar to that of the porphyritic hypersolvus alkali feldspar granite.

The present study reports the preliminary studies of silicate melt inclusions in quartz of mineralized granites from the Pitinga Province. We investigated melt inclusions hosted by quartz phenocrysts of the albite-rich granite and porphyritic hypersolvus alkali feldspar granite from Madeira pluton.

Therefore, the study of melt inclusions could contribute to finding evidence of magmatic immiscibility and characterize the fractionation of fluorine and trace elements (including REE) in the magmatic liquids trapped in quartz crystals of both granitic facies.

Furthermore, based on the premise that the albite-rich granite and porphyritic hypersolvus alkali feldspar granite were derived from liquids that coexisted during at least part of their crystallization (*cf.* Costi *et al.* 2000), and based on the data obtained from the study of melt inclusions, we also evaluated the hypothesis of exsolution of a liquid of peralkaline composition (albite-rich granite) from a parental melt, with a similar composition to the porphyritic hypersolvus alkali feldspar granite.

To help understand the peralkaline melt which gave origin to the albite-rich granite and its associated mineralization, this paper conducted a petrographic and chemical characterization of these quartz-hosted melt inclusions, through studies of microthermometry and very high-temperature muffle furnace, complemented with scanning electron microscopy/energy-dispersive X-ray spectroscopy (SEM/EDS), laser ablation inductively coupled plasma mass spectrometry (LA-ICP-MS), and electron microprobe analyses.

GEOLOGICAL SETTING

The Pitinga Province, located in the southern region of the Guiana Shield (Almeida *et al.* 1981, Gibbs and Barron 1983), belongs to the Tapajós-Parima Province of the Amazonas craton, more precisely in the Uaimiri domain, according to Santos *et al.* (2006).

The northern and southern portions of the Pitinga Province are constituted by calc-alkaline granitoids grouped in the Água Branca suite (Araújo Neto and Moreira 1976) (Fig. 1). These granitoids are the oldest rocks in the region, and they are in contact with volcanic rocks of the Iricoumé Group, with ages between 1.89 and 1.90 Ga (Almeida 2006).

The rocks of this volcanic association are intruded by granite bodies (Simão, Rastro, Bom Futuro, Alto Pitinga and Pedreira), which provide ages similar to those of the rocks of the Iricoumé Group, and they were interpreted as their plutonic equivalents and grouped under the denomination of Mapuera Suite, belonging to the Uatumã Supergroup (Ferron *et al.* 2006). This group of rocks is superimposed by sedimentary and pyroclastic rocks of the Urupi Formation.

Geochronological data on plutonic rocks from Madeira, Água Boa, and Europa granites (Madeira Suite) showed that these are significantly younger than their surrounding volcanic rocks, with ages around 1.83–1.82 Ga (Costi *et al.* 2000, Bastos Neto *et al.* 2014). Hypabyssal tholeiitic sills (1780 ± 3 Ma, Santos *et al.* 2002) and dikes of the Quarenta Ilhas Formation represent late magmatic events. The diabases and basalts of the Seringa Formation (1100 Ma, Veiga Jr. *et al.* 1979) represent the latest magmatic event recorded in the region.

Summary of the geology, petrography, and geochemistry of Madeira Granite

The Madeira granite contains four facies (Costi 2000): amphibole-biotite syenogranite, biotite alkali feldspar granite, porphyritic hypersolvus alkali feldspar granite, and albite-rich granite.

The amphibole-biotite syenogranite is equigranular to porphyritic, with micrographic intergrowths in the matrix of the porphyritic types. This facies is metaluminous, composed of perthitic alkali feldspar (60–75%), quartz (20–30%), plagioclase (~10%), biotite, and hornblende; zircon, fluorite, and opaque phases are accessory minerals. The biotite alkali feldspar granite facies is peraluminous, equigranular, locally porphyritic, and is composed of alkali feldspar (55–60%), quartz (30–35%), plagioclase (0–10%), and biotite (1–5%); albite, fluorite, zircon, opaque phases, and topaz are accessory minerals. The porphyritic hypersolvus alkali feldspar granite is metaluminous to peralkaline, has quartz and K-feldspar phenocrysts and a fine- to medium-grained matrix composed essentially of K-feldspar and quartz. Late intergranular albite, biotite, fluorite, zircon, and opaque phases are accessory minerals.

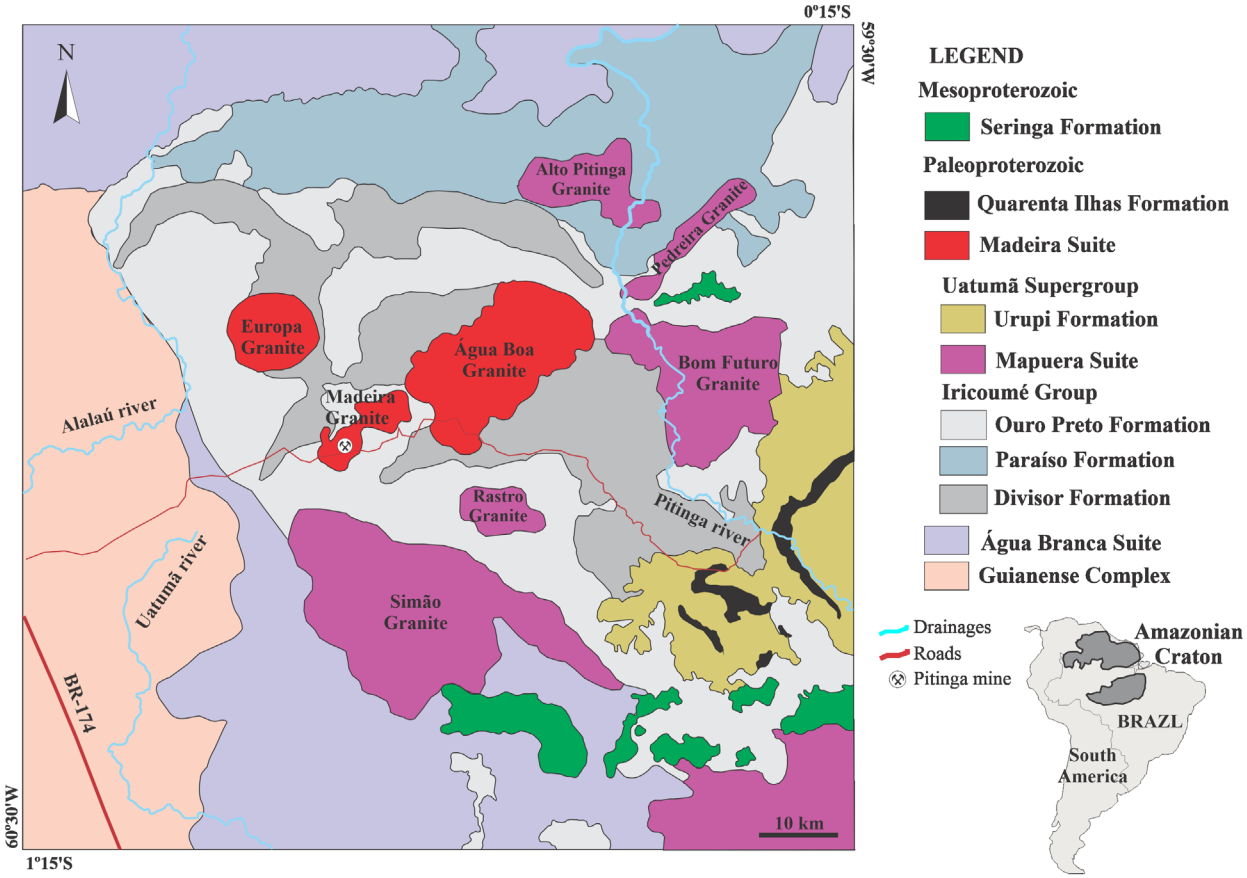

Source: modified from Veiga Jr. *et al.* (1979), Costi (2000), and Ferron *et al.* (2006).
Figure 1. Simplified geological map of the Pitinga Province.

The albite-rich granite (Fig. 2) is subsolvus, aged 1818 ± 2 Ma Pb-Pb zircon (Costi *et al.* 2000), or 1822 ± 22 Ma (Bastos Neto *et al.* 2014) U-Pb zircon, crystallized from an F-rich magmatic fluid, also enriched in Sn, Rb and HFSE. It is composed of a cryolite-bearing core facies, peralkaline, and a border facies, fluorite-bearing, oxidized, peraluminous to metaluminous, generated by autometasomatic processes after crystallization of the core facies (Costi *et al.* 2009).

Petrographic studies indicate that quartz was the first phase to crystallize, at approximately 700°C; the cotectic quartz-alkali feldspar was attained at approximately 650°C, and the solvus of the ternary feldspar and the beginning of albite crystallization, towards the solidus, estimated at approximately 500°C. The albite-rich granite was probably originated by the crystallization of a dense F-rich peralkaline phase, derived from a peralkaline to metaluminous parental magma, by immiscibility (Costi *et al.* 2009).

The hypersolvus alkali feldspar granite, metaluminous to peralkaline, is comagmatic with the albite-rich granite; contact relations indicate that these granites were derived from liquids that coexisted during at least part of their crystallization history (Costi *et al.* 2000).

METHODOLOGY

The samples used in this study were PHR-82a, representative of the core facies albite-rich granite (Fig. 3A), and PHR-179, representing the hypersolvus porphyritic alkali feldspar granite (Fig. 3B), the latter hereafter called porphyritic granite.

For the experimental and microanalytical study of melt inclusions (described below), the samples were prepared as doubly polished thin sections (30-50 µm) and observed by optical microscopy and scanning electron microscopy associated with energy-dispersive spectroscopy (SEM-EDS).

Microthermometric experiments

The purpose of experimental studies of melt inclusions is to reheat the inclusions to the temperature at which they were trapped (homogenization), thus reversing the phase changes that occurred during natural cooling, i.e., crystallization and shrinkage/fluid bubble formation, and then quench the restored trapped composition for further analysis (Danyushevsky *et al.* 2002).

The experiments which involved heating and homogenizing crystallized melt inclusions were performed under atmospheric pressure conditions by three different methods: high-temperature microthermometric stage (temperatures up to 1,350°C); muffle-furnace (temperatures up to 1,200°C); and Air-controlled tubular furnace (temperatures up to 1,200°C).

Heating-stage experiments

Doubly polished sections of representative samples of porphyritic granite and albite-rich granite were heated and quenched on a heating stage coupled to a Leitz microscope. Thus, fragments with crystallized melt inclusions were heated up for homogenization (*liquidus*) and phase transformations were observed and recorded.

The experiments were conducted at Laboratório de Caracterização Mineralógica e Metalogênese — (LCMM/SETEM/

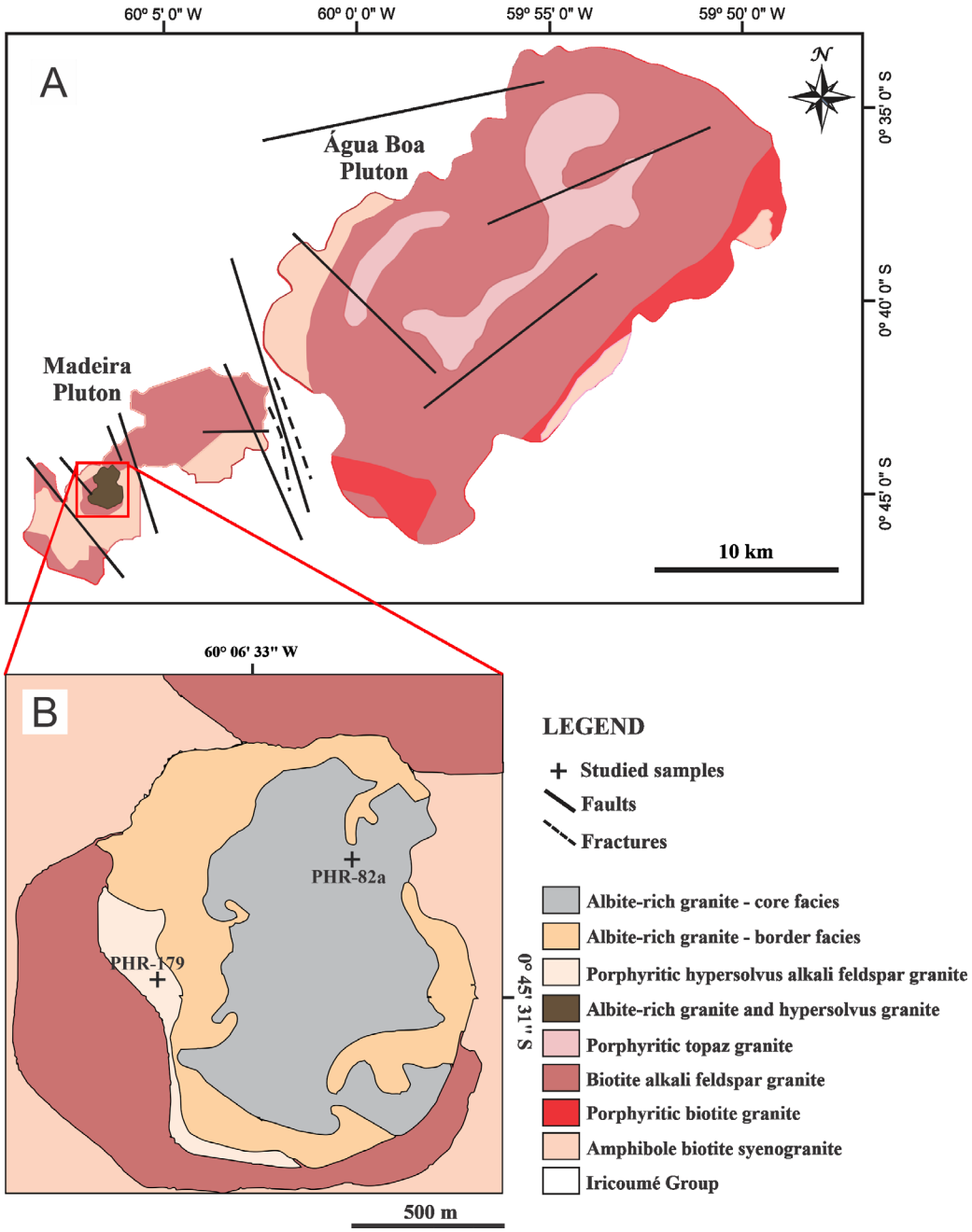

Source: modified from Costi (2000), and Minuzzi (2005).

Figure 2. (A) Geological map of the Madeira and Água Boa plutons. (B) Detailed geological map of the albite-rich granite and porphyritic hypersolvus alkali feldspar granite.

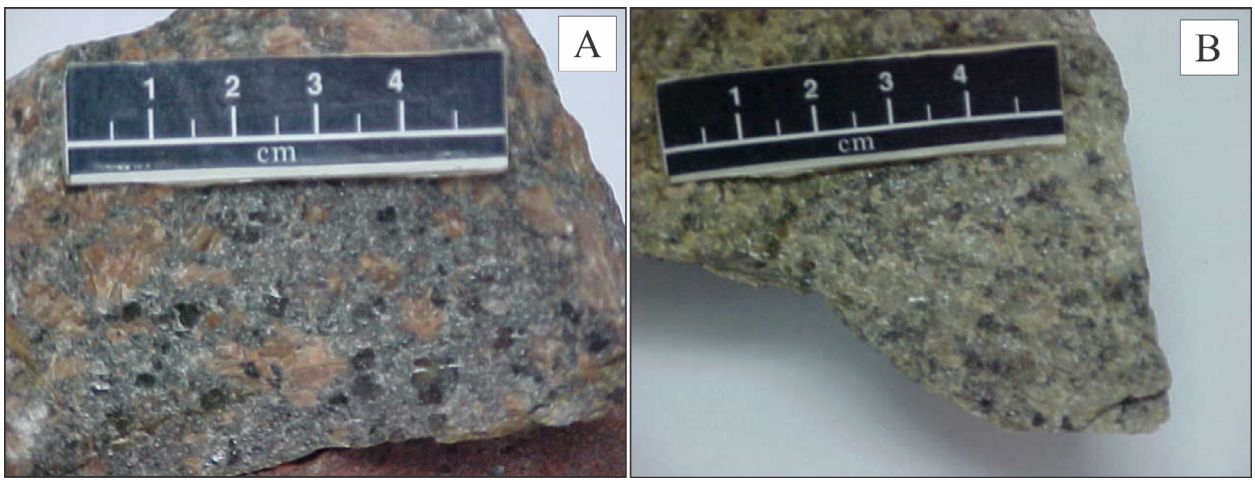

Figure 3. Macroscopic features of the granite samples. (A) Porphyritic granite (PHR-179). (B) Core facies albite-rich granite (PHR-82a).

CDTN) and the sequence of the phase changes and the homogenization temperatures were monitored through a Leica digital camera and an image capture system. The tests were performed under atmospheric pressure and at a heating rate of 4°C/min.

Some melt inclusions showed a refractory behavior (overheating) during the heating tests and were homogenized at temperatures far above the probable liquidus of the granite systems due to the slow kinetics of the felsic silicate melts. Thus, even at temperatures of 1,170°C, some phases were not fully melted, resulting in inclusions not completely homogenized. To avoid this problem, the quenching technique was used soon after the end of the heating experiment (Danyushevsky *et al.* 2002).

Longer muffle furnace experiments

Homogenization temperatures were also determined during longer experiments (bulk heating) in two different muffle furnaces in two Serviço de Minerais Estratégicos e Materiais Avançados/Centro de Desenvolvimento da Tecnologia Nuclear (SEMAV/CDTN) laboratories. Unpolished and doubly polished inclusion-bearing quartz crystals were placed in both porcelain and platinum crucibles and heated at atmospheric pressure to the experiment temperature at a rate of ≈ 1.25°C/min. The samples were quenched by removing the crucibles from the furnace and subjecting them to ambient air.

The heating tests at the Sample Preparation Laboratory were carried out in a QUIMIS Q318M Multi-processed muffle furnace, which can reach temperatures up to 1,200°C. The samples were inserted therein after the desired temperature (800 to 900°C) had been reached and were kept at constant temperatures for six or eight consecutive hours. At the end of the experiment, the crucibles were removed and placed in a desiccator for 30 minutes, and then removed. The inclusions were analyzed under a petrographic microscope.

At the Chemical Analysis Laboratory, samples were heated in a JUNG J30 muffle furnace (220V, 3KW, and 14A conditions), and differently from the procedure followed in the first laboratory, the platinum crucibles were placed in the muffle at a temperature of 85°C only. The temperature of 900°C was reached after 20 minutes of heating and, thereafter, the samples were kept at this temperature for eight hours. After that, the samples were quickly removed from the furnace and placed on top of a refractory block to cool under atmospheric conditions.

Heating in tubular furnace with argon atmosphere

Heating experiments were also conducted at Laboratório de Combustível Nuclear — LABCON/SENAN/CDTN/CNEN at a horizontal tubular EDG 10P-S, with a high flow rate (up to 1,700°C) and argon-controlled flow.

The samples were placed in platinum crucibles on an alumina sample holder (also known as "*barca*") in the furnace at room temperature, which was then sealed. Therefore, the samples were subjected to a gradual temperature increase, minimizing the risk of fractures and/or loss of volatile material.

The air pressure in the internal cylinder/manometer was 50 PSI (= 3,447 bars), the cylinder pressure was 125 PSI in the external shed, and the flow was 24 NL/H (normal liters/hour). Once heating starts, the equipment quickly reaches a temperature of 400°C and, thereafter, the temperature drops to 300°C. The heating rate was 10°C/min. After various temperature surges (known as "*rampas*"), controlled by time and temperature settings, the furnace slowly reached the programmed step (T = 850°C) in approximately 90 minutes.

Once this temperature was reached, the system was controlled for 24 hours under an argon atmosphere. After this period, the furnace was automatically switched off. Following laboratory standard procedures, the system cooled slowly and the furnace was opened for crucible removal after approximately 4 hours, at a temperature of 228°C.

This slow cooling process probably caused the observed recrystallization or nucleation of mineral phases within various inclusions, since the standard quenching technique (400°C/sec.) could not be adopted.

Sample evaluation showed that tubular furnace heating and subsequent very slow cooling did not prevent cracking in several quartz crystals. Moreover, the textural aspect of several melt inclusions does not differ from that resulting from the heating of the inclusions in the muffle furnace.

Scanning electron microscopy/ energy-dispersive X-ray spectroscopy

At Laboratório de Microscopia Eletrônica — LME/SENAN/CDTN/CNEN some analyses of crystallized silicate melt inclusions were carried out in a field emission gun scanning electron microscope (FEG-SEM), Carl Zeiss SIGMA VP, coupled to a microanalysis system consisting of a Bruker Nano GmbH EDS, model XFlash 410-M.

The samples were coated with gold under the following conditions: 30 mA and 40 seconds. The studies in the SEM were conducted to obtain mainly the chemical composition of the mineral phases inside the inclusions.

Laser ablation inductively coupled plasma mass spectrometry

Unexposed melt inclusions were analyzed by LA-ICP-MS at the Mass Spectrometry Laboratory (LEM) of CDTN. The setup includes a laser model NW-213 New Wave, with NdYAG crystal source and 213 nm wave-length, coupled to a Perkin Elmer/SCIEX, model ELAN6100 DRC-e (quadrupole), argon plasma mass spectrometer.

The equipment operated with the following settings:

- Laser: Sample 0.080 mJ; Fluency: 2.81 J/cm^2; Spot: 20-60 Microns; Frequency: 5Hz-10Hz; Energy: 45-80%%; Mode: spot; and 50mL/min of He as carrier gas;
- ICP: Readings: 200; Replicate: 1; Analysis time: 2:33 minutes; Gas: 500 mL/min of Ar; External standards: NIST SRM 610 and NIST SRM 612 glasses.

The chemical analyses were performed on six fragments of doubly polished thin sections that were assembled and glued on glass slides with Araldite. Recommendations of Pettke (2006) were followed in the chemical analysis methodology.

Elements were measured on isotopes (analytes) and the dwell times were: ^{23}Na (8.3.ms), ^{25}Mg (8.3.ms), ^{27}Al (16.6.ms),

^{30}Si (8.3.ms), ^{42}Ca (16.6.ms), ^{45}Sc (16.6.ms), ^{47}Ti (16.6.ms), ^{66}Zn (8.3.ms), ^{69}Ga (16.6.ms), ^{85}Rb (16.6.ms), ^{88}Sr (16.6.ms), ^{89}Y (16.6.ms), ^{90}Zr (16.6.ms), ^{93}Nb (16.6.ms), ^{118}Sn (16.6.ms), ^{133}Cs (8.3.ms), ^{135}Ba (24.9.ms), ^{139}La (16.6.ms), ^{140}Ce (16.6.ms), ^{141}Pr (16.6.ms), ^{146}Nd (16.6.ms), ^{151}Eu (24.9.ms), ^{152}Sm (16.6.ms), ^{155}Gd (24.9.ms), ^{159}Tb (24.9.ms), ^{163}Dy (16.6.ms), ^{165}Ho (16.6.ms), ^{167}Er (16.6.ms), ^{169}Tm (24.9.ms), ^{172}Yb (16.6.ms), ^{175}Lu (24.9.ms), ^{178}Hf (16.6.ms), ^{181}Ta (16.6.ms), ^{208}Pb (16.6.ms), ^{232}Th (16.6.ms) and ^{238}U (16.6.ms).

During the analyses, and based on the diameter of the melt inclusions, variable spot sizes were chosen, 25, 40, 50, or 60 μm. In extreme cases, a spot size of 110 μm was used for the analysis of the total volume of the larger inclusions.

Values ranging from 45% to 80% of the total energy of the laser were also used, and between 5 and 10 Hz of the laser frequency, depending on the characteristics of the inclusions. In general, the greater the inclusion, the better the signal on the spectrometer.

SILLS software version 1.1.0 (Allan *et al*. 2005, Guillong *et al*. 2008) was used to reduce and calculate trace element concentrations in melt inclusions.

Since the surface of the sample was not exposed in the majority of the homogenized silicate melt inclusions, but a distribution occurred at different depths, it was necessary to use a spot that caused the ablation of the entire inclusion, together with a portion of the host crystal. This technique is illustrated in Halter *et al.* (2002).

Thus, for the matrix correction procedures and for calculating the concentrations of the chemical elements, deconvolution of the mixed-signal was necessary with an internal standard.

Applying one of the techniques proposed by Halter *et al.* (2002), in which a predetermined, fixed concentration of an element in the magmatic liquid can be used, it was decided to use the concentrations of Al_2O_3 in bulk rock of the respective granitic rocks as internal standard, starting from the premise that the composition of the trapped liquid in the silicate melt inclusions would correspond to the one of the magmatic liquid during the crystallization of the hosting quartz phenocrysts.

NIST-610 and NIST-612 certified materials were used as quality control throughout the analysis. These standards showed recovery ranging from 80 to 120% under the same conditions of analysis used in the samples (energy, spot diameter, and internal calibration standards).

Detection limits depend on the size of the analyzed inclusion, and thus vary from analysis to analysis.

Electron microprobe analysis

Using polished quartz crystals mount, chemical analyses of exposed melt inclusions were performed by electron microprobe at Laboratório de Microanálises of Universidade Federal do Pará Instituto de Geociências.

The chemical compositions of melt inclusions were obtained using a JEOL JXA-8230 electron microprobe equipped with 5 WDS spectrometers, operating at 15 kV acceleration voltage, 20 nA beam current, focused beam diameter of 5–10 μm depending on inclusion size, and 20-40s counting time for the major elements analyzed. To minimize the loss of Na and F, these elements were measured first. Elements, crystals, and standards used in the electron microprobe analyses were as follows: F (LDE1; fluorite); Na (TAP; sodalite); Mg (TAP; forsterite); Al (TAP; anorthite); Si (TAP; orthoclase); Ca (PETJ; wollastonite); K (PETJ; orthoclase); Fe (LIF; Fe_3O4); Mn (LIF; rhodonite); Ti (LIF; rutile); Sn (PETH; cassiterite); Cl (PETH; sodalite); P (PETH; apatite).

RESULTS

Petrography of melt inclusions

A petrographic study was carried out to describe the morphological characteristics and the distribution of the quartz-hosted crystallized silicate melt inclusions identified in both facies, porphyritic granite and albite-rich granite.

Crystallized melt inclusions occur in various shapes and sizes, birefringent microcrystalline aggregates of silicate minerals with misshapen vapor phases filling the spaces between solids, and rare opaque phases (Figs. 4 and 5).

The inclusions have a mean diameter of 10-20 μm, but some reach sizes up to 120 μm. All identified inclusions were classified as primary (zonal), occurring in clusters aligned with albite, micas, and cryolite crystals that form the snowball texture in the quartz crystals of the albite-rich granite (Figs. 4A and 4B) or are aligned along growth planes arranged parallelly to faces of the euhedral quartz phenocrysts in the porphyritic granite (Fig. 5A). After the heating experiments, homogenized melt inclusions were observed along growth planes on quartz from albite-rich granite (Fig. 4A) and porphyritic granite (Fig. 5A). They form assemblages of melt inclusions (MIA), according to Bodnar and Student (2006). They rarely occur as randomly distributed inclusions.

The dark inclusions are brown to black in color (Figs. 4D, 4E, 5B, 5C, and 5D) and have a granular texture. The occurrence of a bubble (vapor phase) is a common feature in many of them (Figs. 4F, 4G, 5B, and 5F). These bubbles are sometimes distorted, occupying a maximum of 15% of the volume of the inclusion, usually tightened against one of the edges of the cavity.

Some inclusions have solid phases (daughter minerals?) that show a refractory behavior, and do not melt during heating experiments (Fig. 5F).

Composition of mineral phases in crystallized melt inclusions

Before the heating experiments, backscattered electrons (BSE) images were obtained and chemical analyses by EDS were performed in some mineral phases resulting from the crystallization of silicate liquids of both porphyritic granite (Figs. 6A, 6B, 6C, 6D, and 6E) and albite-rich granite (Figs. 6F, 6G, and 6H).

Thus, in the porphyritic granite, the analyses identified the following minerals: fluocerite-(Ce): (Ce, La)F_3; monazite: (Ce, La, Th)PO_4; bastnäsite-(Ce): (Ce, La)CO_3F, containing other elements (Th, Nb, and Ca), including other REE (Y, Nd, Dy,

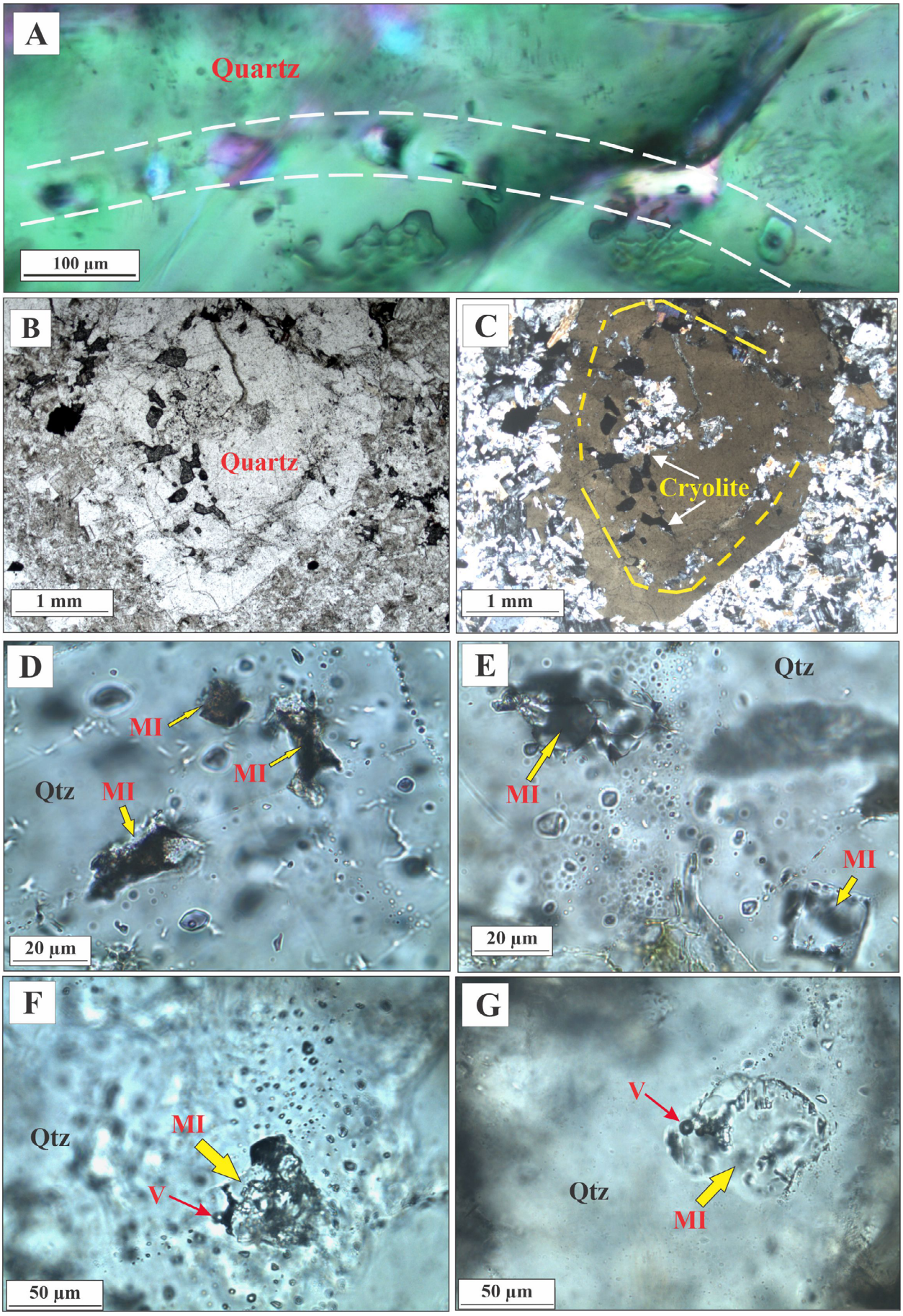

Qtz: quartz.

Figure 4. Silicate melt inclusions in the albite-rich granite. (A) Growth plane of homogenized melt inclusions in a quartz phenocryst. (B and C) Euhedral snowball phenocryst of quartz showing crystallized melt inclusions (MI) distributed (yellow traces) along with mineral phases, mainly albite laths, cryolite and micas. (D–G) Crystallized melt inclusions composed of opaque phases with granular textures (D, E) or microcrystalline aggregates of silicate minerals with misshapen vapor phases (V) filling the spaces between solids (F, G), (red arrow). All photomicrographs in plane-polarized light, except (A) and (C), in crossed nicols.

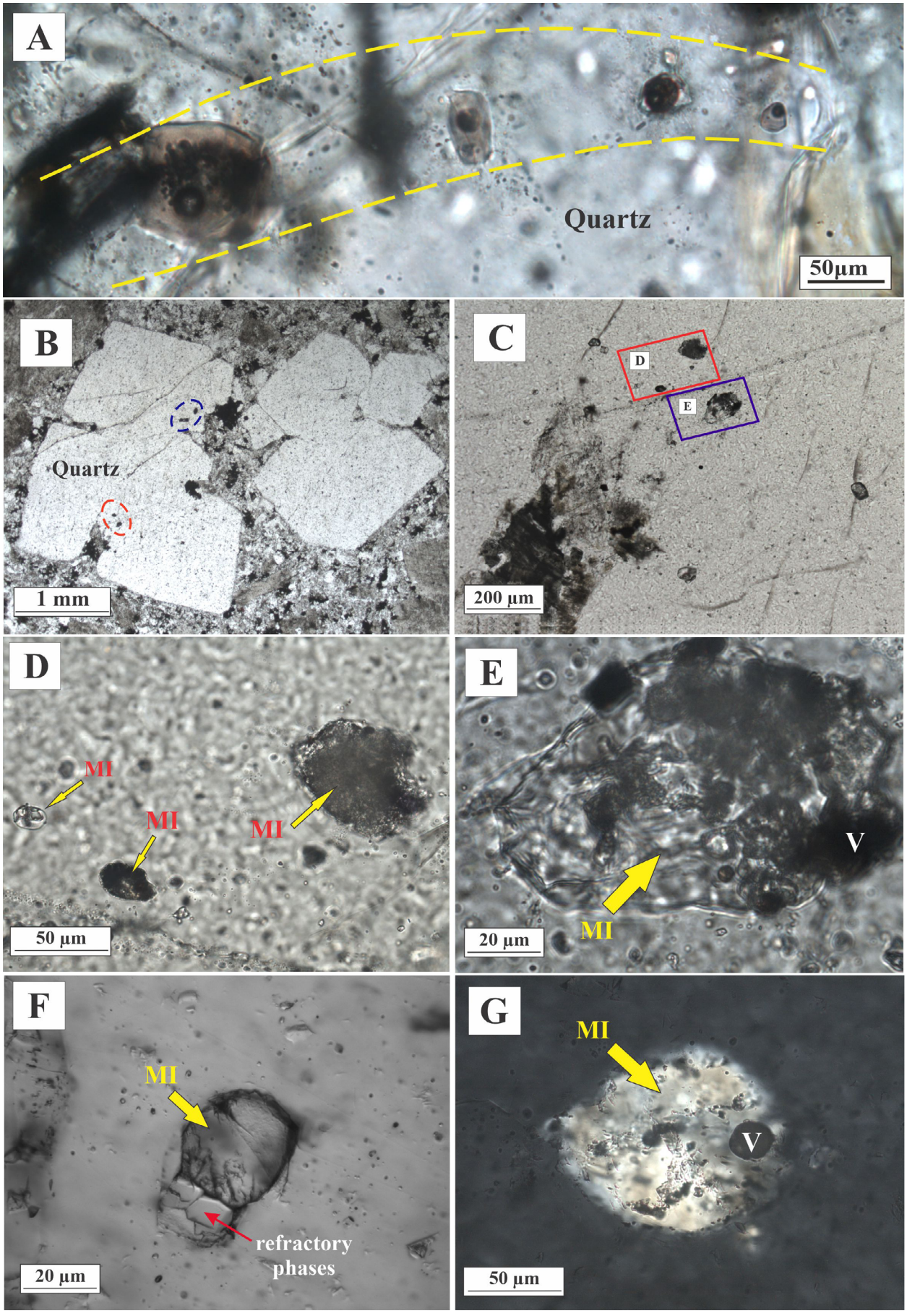

V: vapor bubble. MI: melt inclusions.

Figure 5. Silicate melt inclusions in the porphyritic granite. (A) Growth plane (yellow traces) of homogenized melt inclusions in a quartz phenocryst, after homogenization at 900°C, 1 atm and 8 hours. (B) Quartz phenocrysts in the porphyritic granite with melt inclusions (red and blue circles) near reabsorption features on border of crystals. (C) Expanded area of the B, showing two grouping (D and E) of crystallized melt inclusions. (F) Melt inclusion filled with very high relief crystals (red arrow), which have a refractory behavior during heating experiment. The vapor phase is clearly present in two inclusions (E and G). All photomicrographs in plane-polarized light, except (G), in crossed nicols.

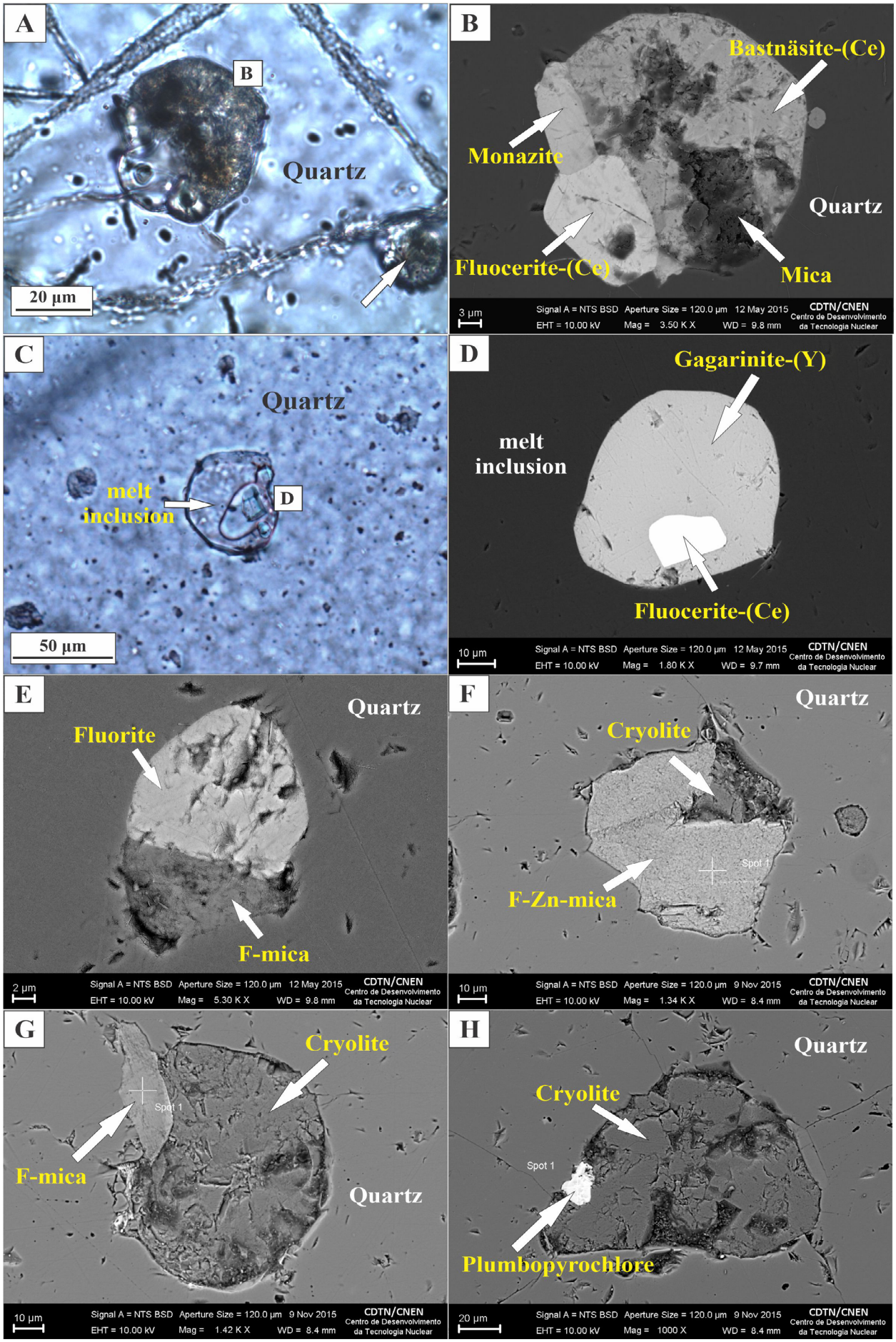

Figure 6. Photomicrographs of crystallized melt inclusions in quartz crystals at room temperature before heating experiments. The crystal phases were identified based on the chemical analyses by EDS-SEM. (A–E) Inclusions in quartz from porphyritic granite. (F–H) Inclusions in quartz from albite-rich granite. Backscattered electron images (B, D–H) and optical images (A, C). In (A) the arrow indicates a similar but smaller inclusion.

Er, Yb); gagarinite-(Y): NaCaY $(F, Cl)_6$; Mica: K $(Mg, Fe)_3$ $(AlSi_3O_{10})$ $(Cl, OH)_2$; and fluorite: CaF_2.

In Pitinga, gagarinite-(Y) occurs associated with the core albite-rich granite, in the massive cryolite zone, at 150-200 meters deep (Pires 2010). This author also identified abundant inclusions of fluocerite-(Ce) in the former, and has interpreted its origin as related to exsolution processes.

The occurrence of gagarinite-(Y), fluocerite-(Ce), and bastnäsite-(Ce) as solid phases in the silicate melt inclusions indicates that the melt that gave rise to the porphyritic granite was already saturated in F, Y, Ce and La, and other REE during the crystallization of quartz phenocrysts. In addition to F, this melt also bears CO_2, leading to the formation of REE fluorocarbonates.

In the albite-rich granite, the mineral phases identified were: cryolite: Na_3AlF_6; plumbopyrochlore: $(Pb, Y, U, Ca)_{2-x}Nb_2O_6(OH)$; F-mica: $K(Fe)_3(AlSi_3O_{10})(F, OH)_2$; F-Zn-mica: $K(Fe, Zn)_3(AlSi_3O_{10})(F, OH)_2$.

Microscope heating-stage experiments

As observed in Fig. 7, the temperatures of 1,039 and 1,065°C are considered a step slightly below the total homogenization of two inclusions of one sample of albite-rich granite. The silicate melt inclusions of porphyritic granite are homogenized at temperatures slightly above 1,091°C (Fig. 8A).

In all the samples, melt inclusions are homogenized once the vapor phase (bubble) and/or spherical globules of different sizes disappear (Fig. 8B). After heating, quenching of some inclusions of porphyritic granite was also observed, and the clear glass inclusions developed a granular texture, with brown color (Fig. 8C) and a shrinkage bubble.

In fact, the very high temperatures reached during the heating experiments of crystalline melt inclusions do not represent the true liquidus temperature of granite systems. Therefore, temperatures of 1,039, 1,065, and 1,091°C are assumed to be "apparent" homogenization temperatures. In Pitinga, for example, the crystallization interval for the albite rich-granite was estimated between ~700–500°C (Costi *et al.* 2009).

According to Thomas and Klemm (1997), microthermometric experiments involving direct observation of inclusions on a heating stage commonly lead to serious overestimation of the homogenization temperature in melt inclusions because homogenization is slow (Roedder 1984a, 1984b, Hansteen 1991, Lowenstern 1995, Student and Bodnar 1996).

The same authors, discussing kinetic techniques in the study of silicate melt inclusions, suggest that, in addition to the possibility of heterogeneous trapping, this kinetic effect may be the reason for the unrealistically high homogenization temperatures (1,000°C) reported for granitic melts in the literature (*cf.* Lukkari *et al.* 2009).

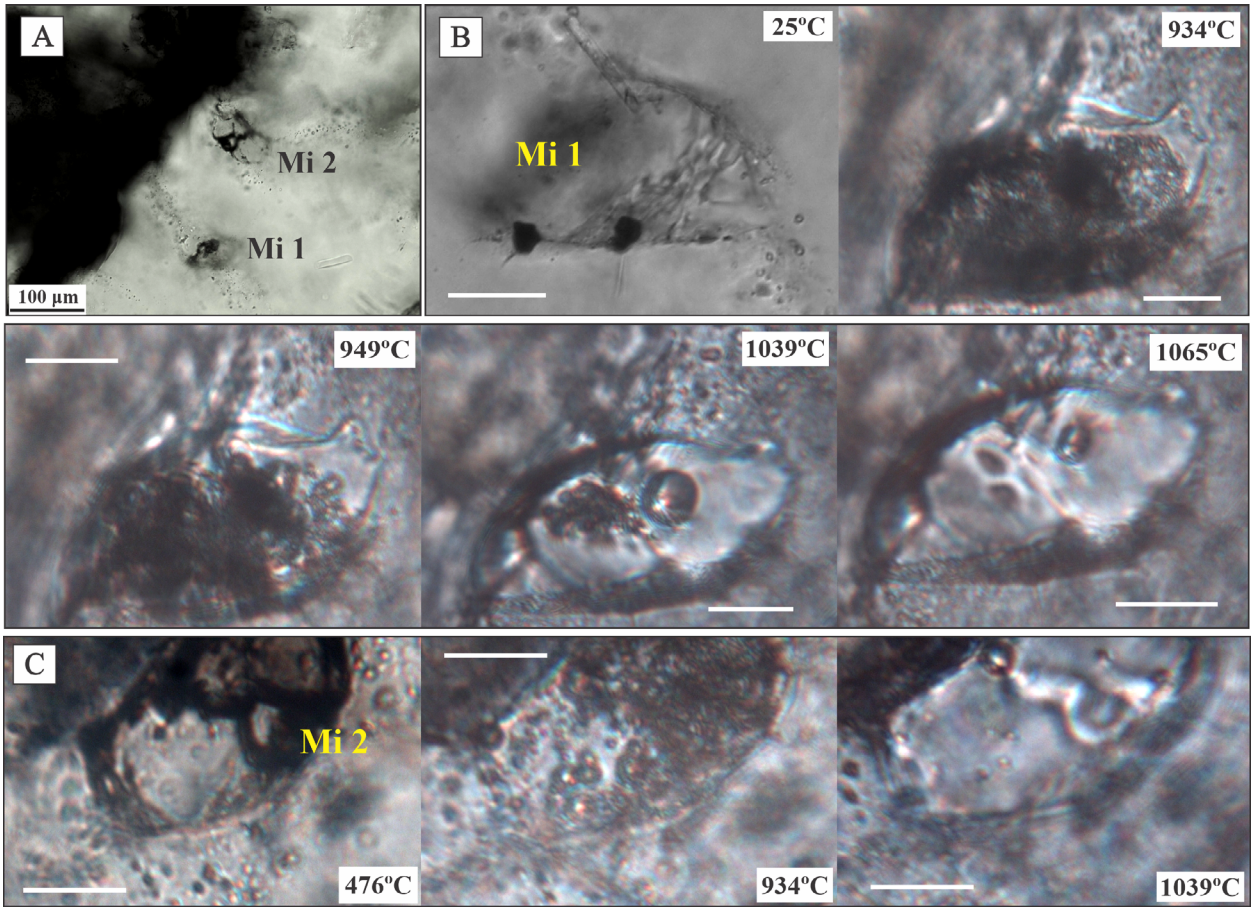

Figure 7. (A) Crystallized melt inclusions in quartz from the albite-rich granite at room temperature before homogenization. (B and C) Phase transformations in composite melt inclusions (Mi) 1 and 2, respectively, during heating stage experiments. The temperatures of (B) 1,065°C and (C) 1,039°C are considered a step slightly below the total homogenization of inclusions 1 and 2. Scale bars are 50 µm, except in (A).

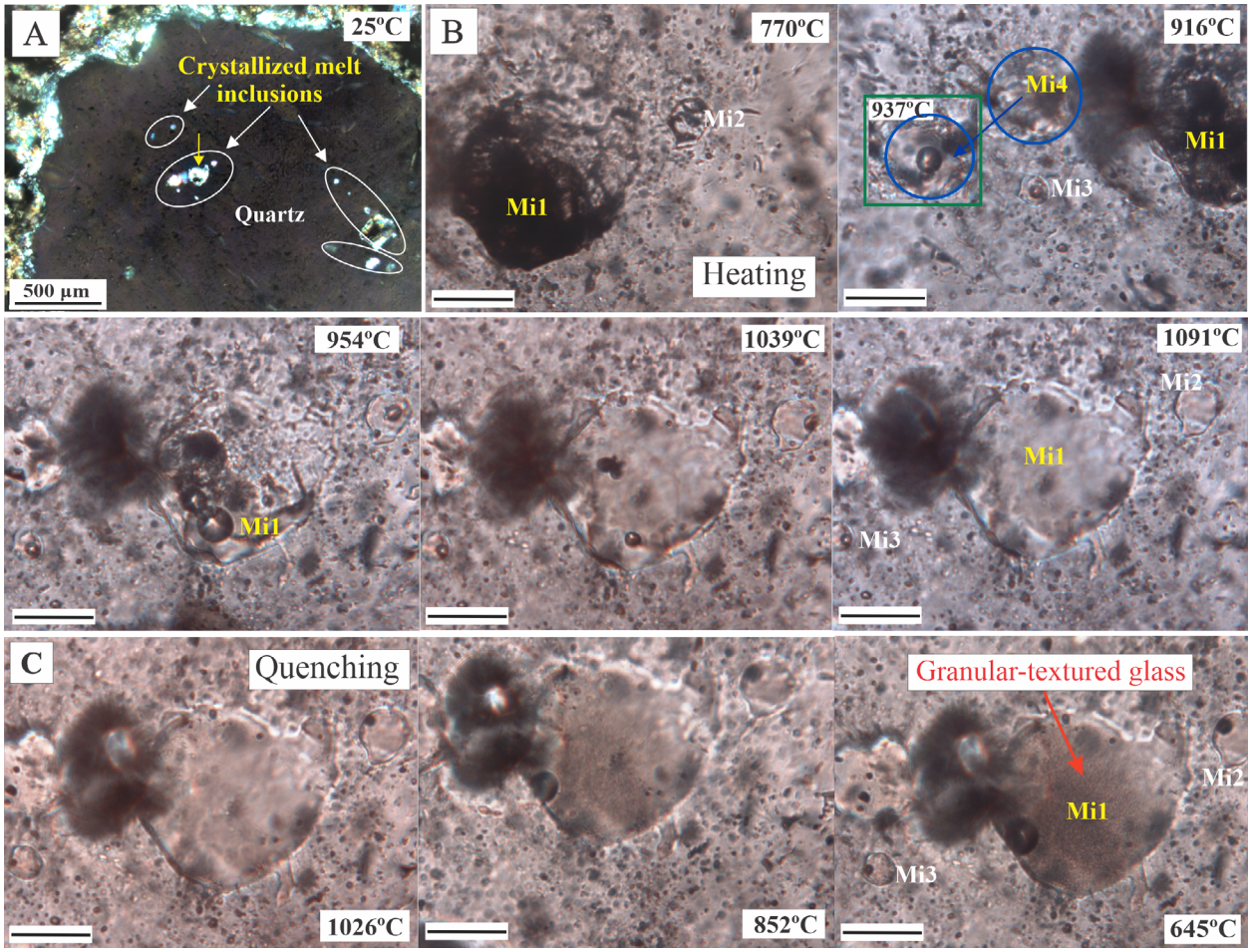

Figure 8. Melt inclusions (Mi) in quartz from the porphyritic granite. (A) A cluster of quartz-hosted crystalized melt inclusions (inside white ellipses) at room temperature before homogenization. The yellow arrow marks the melt inclusion 1. (B) Phase transformations during the heating and homogenization experiments on the Leitz heating stage. At 916°C, the insert in the middle left corner is a close-up of the out of focus inclusion Mi4, photographed at 937°C. The temperature of 1091°C is considered the total homogenization of melt inclusions 1, 2 and 4. (C) The subsequent quenching of inclusions shows the first nucleation of a vapor bubble at 1,026°C, as registered in inclusions 2 and 3. At 645°C the glass inclusions show a typical granular texture and a shrinkage bubble. Scale bars are 50 µm, except in (A).

Bulk heating experiments

Although bulk heating does not allow visual control during the experiment, this method is often preferred compared to the heating stage (e.g. Skirius *et al.* 1990) because of the reaction inertia of viscous felsic melts (Agangi *et al.* 2015).

Furthermore, when the desired temperature was reached, the samples were kept in the furnace for 6, 8, or even 24 hours. Several authors have shown, based on the results of a study of synthetic silicate melt inclusions, that 24-hour periods (duration of heating) provide a more reliable homogenization temperature (e.g. Student and Bodnar 1999).

The melt inclusions in phenocrysts and crystals (matrix) of quartz from the porphyritic granite were heated in different furnaces and reached maximum temperatures of 850°C, 1 atm and 24 hours in a tubular furnace (Figs. 9A, and 9B); 900°C, 1 atm and 8 hours in a muffle furnace (Figs. 9C, 9D, 9E, 9I, and 9J); and 850°C, 1 atm and 6 hours in a muffle furnace (Fig. 9F).

The magmatic inclusions in quartz phenocrysts from the albite-rich granite were subjected to bulk heating and quenching (Figs. 10A, 10F, and 10J) in a muffle furnace at 900°C, 1 atm and 8 hours. Some heating runs were made in a tubular furnace at 850°C, 1 atm, 24 hours (Fig. 10I).

In this study, the homogenization temperature used (850–900°C) was high enough to homogenize the crystallized phases in the inclusions, and avoid overheating and melting of the host mineral.

These muffle furnace experiments were important to try to establish a more consistent homogenization temperature and to obtain homogenized inclusions (glass) appropriate for the chemical analysis of trace elements. After all the experiments carried out, the temperature of 900°C proved to be the most suitable for silicate inclusions (Th), despite being well above the liquidus temperature of the albite-rich granite from Pitinga. Most of the crystalline melt inclusions certainly reached total homogenization at 900°C. However, after quenching, they showed textures strongly suggestive of immiscibility, as will be discussed below.

Textures of the melt inclusions after quenching

After homogenization and quenching, the melt inclusions showed different types of textures according to the presence or predominance of different phases. Instead of a completely homogenized inclusion, the quenching process caused the

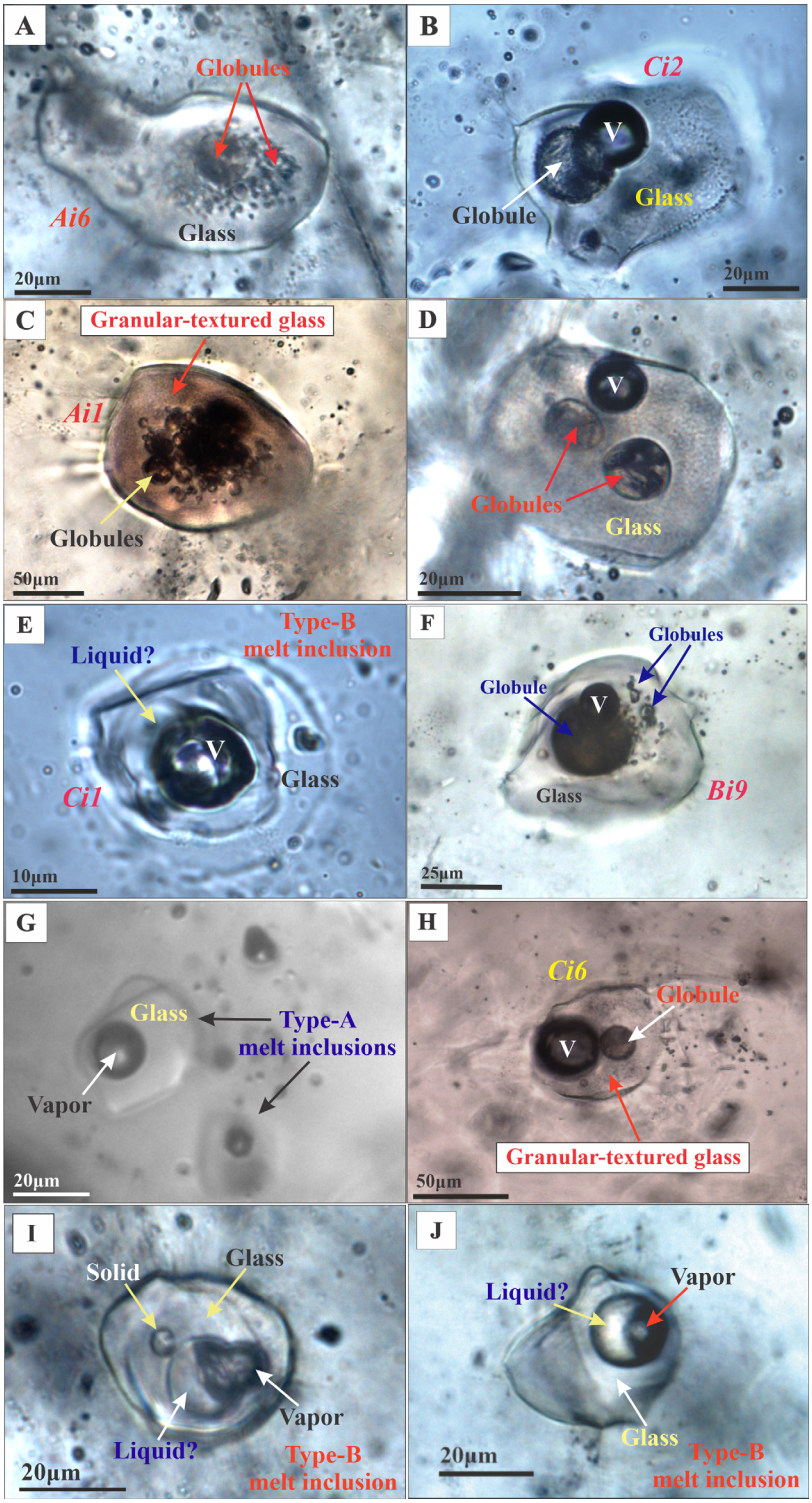

V: vapor bubble.

Figure 9. Melt inclusions in phenocrysts and crystals (matrix) of quartz from the porphyritic granite after bulk heating and quenching experiments, except the inclusion in (H), which was submitted to heating in microthermometric stage. (A and B) Composite melt inclusions after homogenization at 850°C, 1 atm and 24 hours in tubular furnace. These inclusions are composed of glass, globules of different sizes, and a vapor phase. (C) Granular-textured glass inclusion, showing the typical brown, granular appearance, after heating at 900°C, 1 atm and 8 hours. In addition, the spherical globules are concentrated at the center of inclusion. (D) This inclusion shows a vapor phase, a granular-textured glass, and the two globules seem to represent a coalescence of smaller globules. (E) B-type melt inclusion after homogenization at 900°C, 1 atm and 8 hours. It is composed of colorless glass, one liquid (?) phase, and a vapor bubble which occupies up to 40% vol. (F) Inclusion heated to 850°C for 6 hours. Magmatic emulsions inclusion (Davidson 2004), showing preferential segregation of emulsion to one side of the inclusion. (G) Typical A-type melt inclusions, consisting of a colorless glass and a shrinkage vapor bubble, after heating and quenching at 850°C, 1 atm Ar, and 24 hours in tubular furnace. (H) This inclusion was heated to 1,073°C (Th) in microthermometric stage. It is similar to inclusion in (B), consisting of a granular-textured glass, a single central spherical globule, and a vapor bubble of about 30 vol percent. (I and J) These inclusions were trapped in quartz crystals of matrix from porphyritic granite, and could represents the most evolved melt at the final stage of crystallization of this granite. Both are B-type melt inclusions after heating at 900°C, 1 atm and 8 hours. These inclusions consist of a silicate glass, one liquid (?) phase, and one vapor bubble representing, probably, a H_2O- and F-rich phase. A-type and B-type melt inclusions according to terminology of Thomas (2000). Composite and granular-textured glass, according to Davidson (2004). *Ci9, Ai6, Bi9*, etc.: selected melt inclusions analyzed by LA-ICP-MS (compositions are in the Tab. 1). All photomicrographs in plane-polarized light.

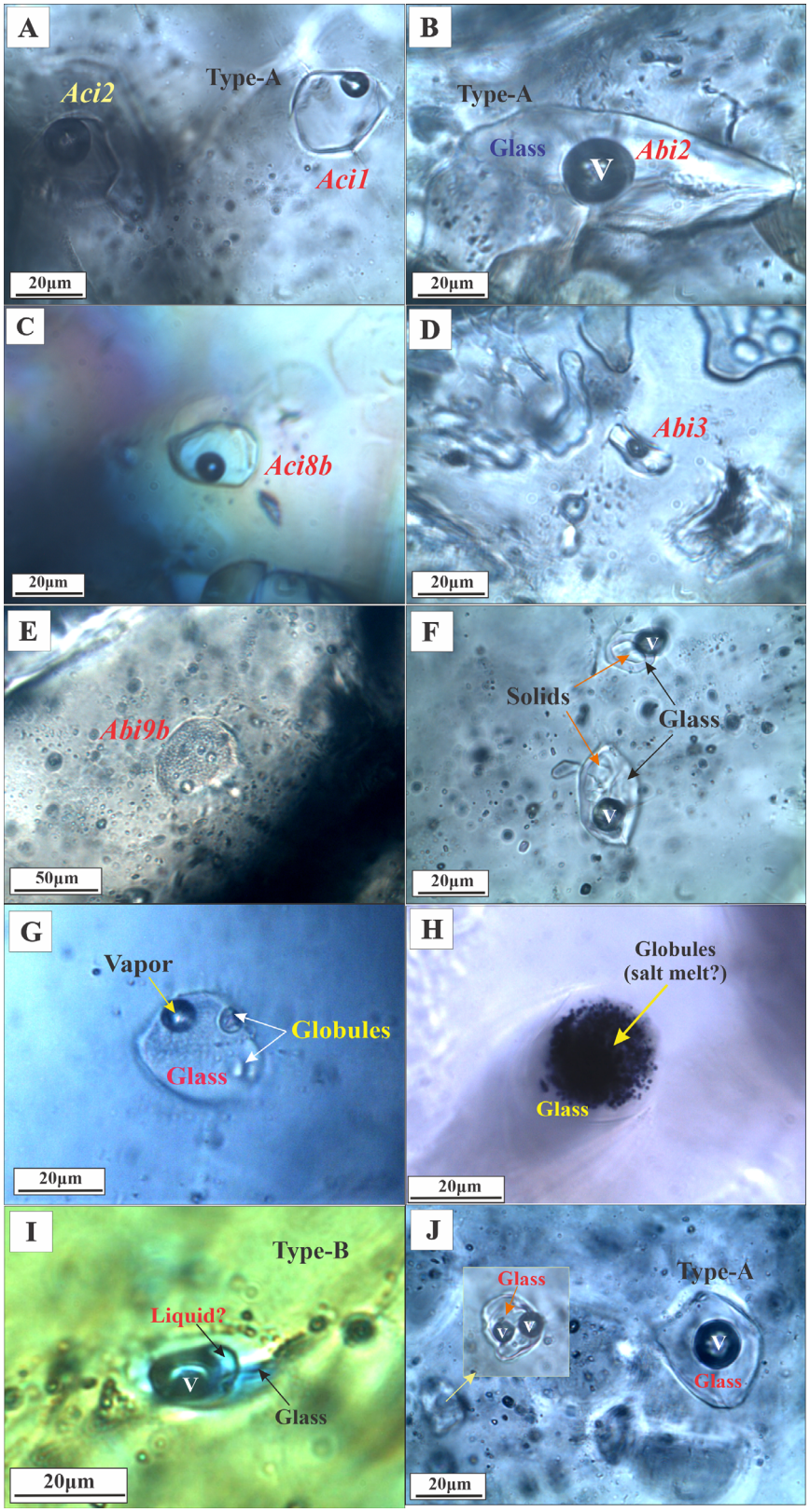

V: vapor.

Figure 10. Magmatic inclusions in quartz phenocrysts from the albite-rich granite, after (A–F; I–J) bulk heating and quenching and (G–H) heating stage experiments. The inclusions (A–F, and J) were heated in muffle furnace at 900°C, 1 atm for 8 hours. Heating stage experiments carried out in the inclusions (G) and (H) reached a maximum temperature of 948 and 1,065°C, respectively. The inclusion (I) was heated in tubular furnace at 850°C, 1 atm, 24 hours. (A-D) These inclusions (A-type, Thomas 2000) are common in the albite-rich granite, and are composed of colorless silicate glass and a shrinkage bubble. (E–H) These inclusions are composite inclusions (Davidson 2004), consisting of a clear silicate glass, with granular texture in (E) and (G), a vapor phase (F–G), and spherical globules of variable dimensions and proportions. The inclusion (H) consists of a high amount of black microcrystalline aggregates (~80% vol.) suspended in the glass "matrix". (F) The two inclusions show three phases: a clear glass, a vapor, and a solid phase that nucleated (daughter mineral?) after quenching. (I) A B-type melt inclusion (Thomas 2000) representing volatile-rich phases (H_2O, F) in the albite-rich granite. (J) Association of a A-type inclusion (right) and a composite inclusion (left), which is a close-up of the out of focus inclusion in the insert in the middle left side of photomicrograph. Note that this latter inclusion has two shrinkage bubble. *Aci1*, *Aci2*, etc.: selected melt inclusions analyzed by LA-ICP-MS (compositions are in the Tab. 2). All photomicrographs in plane-polarized light, except in (C) and (I), in crossed nicols.

separation of phases that, according to several authors (Roedder 1979, Thomas *et al.* 2000, Davidson and Kamenetsky 2001, Kamenetsky *et al.* 2003, Davidson 2004, Student and Bodnar 2004, Bodnar and Student 2006, Thomas *et al.* 2006b, Thomas and Davidson 2013), are products of magmatic immiscibility.

After the heating experiments, we could observe three melt inclusion types in quartz, characterized by contrasting textural and compositional features:

- Melt inclusion A-type, consisting of colorless glass with a vapor bubble with a volume of about 5-10%;
- Melt inclusion B-type, with large shrinkage-induced bubbles with volumes of about 30–40%. The shrinkage bubbles of the B-type melt inclusions are multiphase, containing aqueous liquid, vapor, and, in some cases, a crystalline precipitate in the liquid phase. The liquid and the vapor phases are assumed to have exsolved during or a few hours after quenching (Lukkari *et al.* 2009).

This nomenclature was proposed by Thomas *et al.* (2000), who described that B-type inclusions would represent a volatile-rich melt (H_2O, F, CO_2), while A-type inclusions are low in volatiles.

The third type, apparently more abundant in all the inclusions studied, is described as composite melt inclusion (Davidson and Kamenetsky 2001, Davidson 2004).

The inclusions trapped in the quartz phenocrysts of porphyritic granite, at room temperature, display composite texture, in which the vapor phase (shrinkage bubble) may (Figs. 9B, 9D, 9F, and 9H) or not (Figs. 9A and 9C) be present. Another striking feature of these inclusions is the occurrence of globules of different sizes within the individual inclusions, which may be larger (Figs. 9B, 9D, and 9F) or smaller than the vapor phase. In addition, within the inclusion, globules may vary considerably in size (Figs. 9A, 9C, and 9F). According to Davidson (2004), in contrast to shrinkage bubbles, which probably contain only low-pressure water vapor, globules refer to higher density phases which may represent co-trapped, and therefore, immiscible phases.

The globules are frequently concentrated near the core of the inclusions, coalescing with the larger globule (Figs. 9A, 9C, and 9F).

The glass phase is present in all inclusions. However, in composite inclusions, it has a granular texture (Figs. 9B, 9C, and 9D), called granular-textured glass, which may have a brown color locally.

A-type (Fig. 9G) and B-type (Fig. 9E) inclusions are found in smaller proportions. Both consist of clear glass, predominant in the case of A-type, whereas in B-type the volatile-rich phase (F, H_2O) occupies virtually 50% of the volume of inclusion.

On the other hand, the magmatic inclusions trapped in crystals of porphyritic granite matrix are of B-type, showing four (Fig. 9I) or three phases (Fig. 9J) at room temperature. The silicate glass is always clear, and the phase separation into glass, liquid, and vapor occurred during quenching. In Fig. 9I, a solid (daughter mineral?) is observed inside the liquid phase. In both inclusions (Figs. 9I and 9J), the volatile rich-phase occupies about 50% of the total inclusion volume.

In albite-rich granite, the predominant inclusions are of A-type (Thomas 2000) (Figs. 10A, 10B, 10C, 10D, and 10J). B-type inclusions (Fig. 10I) occur in a small amount. Apparently, they may have decrepitated during the heating experiments due to their high volatile content. Composite inclusions (Davidson 2004), with a granular texture, also occur within some quartz phenocryst (Figs. 10E, 10F, 10G, and 10H), associated with A- and B-type inclusions.

Some inclusions show a texture formed by fine dark microcrystalline aggregates immersed in clear glass (like emulsions) (Fig. 10H). These dark globules have been described as representing salt melts by several authors (e.g. Kamenetsky *et al.* 2003, Davidson 2004).

B-type inclusions (Thomas 2000) in quartz of the porphyritic granite matrix (Figs. 9I and 9J) probably represent the magmatic fraction richest in fluxing components (H_2O, F, Cl, SO_4^{2-}, CO_3^{2-}, etc.), and the most evolved of the parental magma that gave rise to porphyritic granite. At this stage of crystallization, a peralkaline fraction could be separated by immiscibility, generating an evolved melt, F- and H_2O-rich, giving rise to the albite-rich granite.

Trace element analyses of melt inclusions by LA-ICP-MS

Chemical analyses of thirty-six elements (see description of LA-ICP-MS technique) were performed on melt inclusions. Due to raw data reduction by SILLS software, the best results were obtained in the incompatible trace elements, such as HFSE (Nb, Ta, Zr, Hf, Pb, Th, U), LILE (Rb, Cs, Sr, Ba), and REE (see Tabs. 1 and 2).

Typical diagrams of transient signals generated during sample ablation and chemical analysis of analytes are shown in Fig. 11. The analyses of the inclusions Bi9 (Fig. 11A) and Ai1 (Fig. 11B) are representative of the porphyritic granite, while the inclusions Abi9b (Fig. 11C) and Aci1 (Fig. 11D) represent the albite-rich granite.

The Bi9 inclusion (Fig. 9F) shows three distinct phases, predominantly clean glass, in addition to a shrinkage bubble, and a massive globule surrounded by smaller globules. The diagram (Fig. 11A) suggests that the two solid phases have been analyzed and their spectra are clearly separated. The Ai1 inclusion (Fig. 9C), on the other hand, shows a spectrum indicative of a faster analysis, probably because the inclusion should have a smaller volume and/or the laser crossed the inclusion more quickly.

The Abi9B inclusion, from the albite-rich granite, apparently behaved as two phases, as shown by its signal diagram. The morphological characteristics of this inclusion (Fig. 10E) indicate that it is formed by glass with a homogeneous nodular texture. The Aci1 inclusion (Fig. 10A) is an A-type inclusion, with a predominant colorless glass phase and a shrinkage bubble occupying ≈ 20% vol. Its signal diagram (Fig. 11D) demonstrates a two-phase behavior, similar to previous inclusions.

Although the transient signal diagrams suggest an individual analysis of the present phases, the inclusions were analyzed by using laser beam sizes slightly larger than its maximum

Table 1. LA-ICP-MS data (concentrations in ppm) for individual quartz melt inclusions from porphyritic hypersolvus alkali feldspar granite (Sample PHR-179).

m.i.	*Ci2*	*Ci1*	*Ci5*	*Ci6*	*Bi1*	*Bi2*	*Bi3*	*Bi6a*	*Bi9*	*Ai3a*	*Ai3*	*Ai12*	*Ai8a*	*Ai6*	*Ai19*	*Ai20*	*Ai2*	*Ai1*
Rb^{85}	6,410	5,593	5,100	5,430	1,850	1,216	1,114	1,340	4,169	bdl	2,796	5,484	10,577	2,932	2,337	2,204	3,861	4,132
Y^{89}	173	350	1,459	2,791	bdl	bdl	22	233	29,403	1,670	47	40	2,408	321	140	167	126	129
Zr^{90}	691	1,012	201	304	9	bdl	218	94	215	bdl	588	169	bdl	675	bdl	306	55	55
Nb^{93}	159	145	250	99	bdl	107	25	10	186	bdl	153	55	184	104	61	87	76	68
Sn^{118}	14	bdl	29	433	69	bdl	92	59	31	bdl	117	bdl	bdl	65	16	54	31	29
Cs^{133}	312	167	2,074	216	bdl	bdl	bdl	64	654	2,527	121	255	4,284	141	166	191	139	202
La^{139}	34.8	97.5	95.7	136.7	bdl	bdl	bdl	28.1	bdl	bdl	65.47	40.8	bdl	29.1	8.5	29.2	14.7	9.6
Ce^{140}	150.7	109.2	262.7	600	bdl	bdl	4.1	47.7	303.5	4338	52.2	34.8	bdl	43.1	102.7	34.5	45.5	26.1
Pr^{141}	163	277.9	2,850.9	3,808.2	40.1	42.4	20.3	520.5	7,978	bdl	56.3	161.2	1,886	128.6	254.3	1,146	152.9	117.7
Nd^{146}	154.4	263.2	2,699.4	3,340.7	37.9	40.2	19.2	492.4	7,552	bdl	53.2	152.5	1,782	121.4	241.2	1,083	145.7	112.2
Eu^{151}	16.5	43.2	370.3	823.5	21.5	bdl	5.5	407.3	218.4	2,295	6.3	34.1	1,203	10.9	22.9	4.7	18.2	14.7
Sm^{152}	50.9	81.2	3,145.7	3,873.1	310.3	bdl	47.1	294.1	907.2	14,557	18.8	14.4	4,889	89.2	78.1	46.1	70.9	64.8
Gd^{155}	8.4	13.2	bdl	16.9	bdl	bdl	bdl	34.6	bdl	2,985	0.6	bdl	bdl	bdl	bdl	bdl	bdl	bdl
Tb^{159}	20.6	bdl	70.9	744.7	bdl	bdl	bdl	288.1	847.8	4,630	5.2	bdl	bdl	31.3	9.1	bdl	17.6	17.4
Dy^{163}	7.7	165.5	bdl	789,9	46.7	92.7	bdl	273.7	216.4	5,565	4.7	95.3	5210	22.3	bdl	0.73	15.1	20.6
Ho^{165}	bdl	4.7	52.1	134.7	24.9	48.1	12.1	22.44	8.8	bdl	1.2	17.7	bdl	9.59	bdl	22.1	3.17	4.3
Er^{167}	18,6	37.6	547.6	779.7	501.3	401.7	bdl	3,231.5	1,230	14,086	8.3	168.7	bdl	57.5	14.5	63.1	22.9	26.1
Tm^{169}	9.6	14.8	222.4	151.4	bdl	bdl	5.36	111.4	3,993	bdl	1.4	bdl	635	7.7	0.9	9.6	3.7	5.9
Yb^{172}	65.4	65.1	7,214.1	415.1	bdl	133.7	bdl	16,648	414.4	bdl	7.4	273.3	1,214	29.9	bdl	bdl	10.7	15.8
Lu^{175}	2.41	29.4	87.4	54.6	35.1	69.1	bdl	95.93	334.7	1,083	1.5	6.48	bdl	4.7	bdl	6.4	1.5	2.3
Hf^{178}	8	135	845	365	bdl	633	118	105	695	bdl	13	256	bdl	25	bdl	19	13	13
Ta^{181}	532	2,366	6,829	8,094	171	bdl	bdl	179	1,026	7,859	237	831	3,005	191	79	203	178	163
Pb^{208}	23	bdl	11	6	bdl	bdl	7	29	bdl	bdl	15	39	169	8	bdl	4	6	3
Th^{232}	24	bdl	12	6	bdl	bdl	7	29	bdl	bdl	15	41	171	8	bdl	4	6	4
U^{238}	29	72	bdl	59	bdl	bdl	51	48	450	3287	18	74	2075	18	11	27	6	7

bdl: below detection limit. Detection limits depend on the size of the analyzed inclusion, and thus vary from analysis to analysis; m.i.: melt inclusion identification number; total number of analyses = 35.

Braz. J. Geol. (2021), 51(4): e20210011

Table 2. LA-ICP-MS data (concentrations in ppm) for individual quartz melt inclusions from albite-rich granite (Sample PHR-82a).

m.i.	*Abi2*	*Abi3*	*Abi8*	*Abi9a*	*Abi9b*	*Abi10a*	*Abi10b*	*Abi12*	*Aci1*	*Aci2*	*Aci8b*
Rb^{85}	10,748	10,574	32,398	5,679	20,192	11,253	8,544	12,210	20,501	5,738	27,697
Y^{89}	345	66	898	65	1,011	210	237	614	450	639	492
Zr^{90}	2,801	3,515	bdl	1,624	13,915	1,846	1,838	2,816	4,504	2,936	4,244
Nb^{93}	1,189	1,009	808	2,002	4,017	631	750	1,732	2,813	5,306	2,229
Sn^{118}	2,554	3,706	5,592	8,128	2,647	428	12	7,442	2,666	7,782	3,106
Cs^{133}	263	1,132	bdl	bdl	3530	643	814	617	2,,892	736	3,356
La^{139}	2,125.6	404.1	2,688.2	1,300.8	1,037.9	195.6	314.1	503	564.4	1,033.8	bdl
Ce^{140}	1244.2	1,623.4	539.4	bdl	2,741	467.1	571.8	4,497	2,337.7	1,924.9	bdl
Pr^{141}	29.1	bdl	bdl	1,026.2	625.1	53.1	43.5	59.7	bdl	171.9	1967.1
Nd^{146}	27.7	bdl	bdl	980.8	597.5	50.9	41.7	57.3	bdl	165.1	bdl
Eu^{151}	5.6	bdl	292.1	bdl	59.2	4.5	24.3	10,7	bdl	18.3	bdl
Sm^{152}	57.9	2,198.7	6,475.9	11,775	158.4	bdl	bdl	60.8	1244.8	46.4	bdl
Gd^{155}	bdl	602.9	bdl	bdl	bdl	bdl	bdl	bdl	bdl	bdl	bdl
Tb^{159}	39.8	641.3	329.6	bdl	51.4	bdl	68.9	84.7	1276.9	35.9	bdl
Dy^{163}	66.1	bdl	3,326.8	1484.6	36.8	bdl	bdl	131.5	bdl	43.6	bdl
Ho^{165}	25.7	bdl	bdl	bdl	25.1	10.1	bdl	50.7	bdl	19.9	bdl
Er^{167}	220.1	148.6	943.7	bdl	235.9	42.4	81.3	356.9	118.9	186.1	bdl
Tm^{169}	37.1	bdl	26.1	903.7	64.5	11.7	0.9	54.4	bdl	35.1	bdl
Yb^{172}	122.8	44.2	bdl	bdl	256.6	36.9	bdl	166.7	1,662.9	139.9	bdl
Lu^{175}	21.8	280.1	bdl	637.2	60.8	12.8	bdl	24.5	61.9	25.1	bdl
Hf^{178}	129	bdl	656	bdl	367	66	66	131.4	bdl	127	bdl
Ta^{181}	232	2,034	75,705	6,347	bdl	18,393	2,641	3,988	2,684	3,138	5,943
Pb^{208}	107	374	28	bdl	453	67	75	231	572	651	167
Th^{232}	113	394	30	bdl	481	72	80	247	614	699	179
U^{238}	bdl	bdl	bdl	bdl	51	18	bdl	36	bdl	58	573

bdl: below detection limit. Detection limits depend on the size of the analyzed inclusion, and thus vary from analysis to analysis; m.i.: melt inclusion identification number; total number of analyses = 46.

diameter, so that the concentrations of the chemical elements refer to the bulk inclusion, regardless of its textural aspect and present phases. According to Halter *et al.* (2004), only complete ablation of the inclusion provides a representative analysis of the trapped melt.

The LA-ICP-MS analyses plotted in trace element correlation diagrams (Fig. 12) demonstrate that the concentrations of all elements are higher in the inclusions of the albite-rich granite than in the porphyritic granite. Besides that, the analyzed elements that most clearly show a positive correlation are Sn, Nb, Zr, Th, Rb, and Y.

The obtained analyses allow us to observe the following: the Rb vs Cs diagram (Fig. 12C) displays a clear compositional overlap, that is, the melts trapped in quartz crystals of granites had a similar variation in contents of Rb and Cs. This behavior generated a very strong positive correlation trend. The two other diagrams with a clear compositional overlap are LREE vs Y (Fig. 12G) and HREE vs Y (Fig. 12H). The light and heavy rare earth elements show positive correlation trends with Y, but the distribution of the REE in porphyritic granite inclusions is wider, occupying the extremes in linear trends.

The second group of analyses shows that the silicate melt inclusions trapped in porphyritic granite and albite-rich granite occupy well-defined fields in correlation diagrams, and the inclusions from the albite-rich granite are richer in Nb (Fig. 12A), Rb (Fig. 12B), Zr (Fig. 12D), Th (Fig. 12E), and Y (Figs. 12G and 12H), in addition to Sn. Consequently, the elemental distribution evidences a compositional gap between two fields, marked mainly by contrasts in Sn concentrations.

Note that important trace elements, such as Rb, Cs, Zr, and Th, are strongly enriched in the albite-rich granite melt. On the other hand, it is noteworthy that the rare earth elements were not enriched in the melt that gave rise to this granite.

The plotted data in Fig. 12E show two populations of melt inclusions with different textural aspects. The population in the lower-left corner of the diagram (dotted field) is formed by composite inclusions (Davidson 2004), rich in microcrystalline spherical globules, and represents the inclusions of porphyritic granite. The other group on the upper right side (dashed field) represents a set of glassy, and Th- and Sn-rich A-type inclusions (Thomas *et al.* 2000), characterizing the inclusions of albite-rich granite.

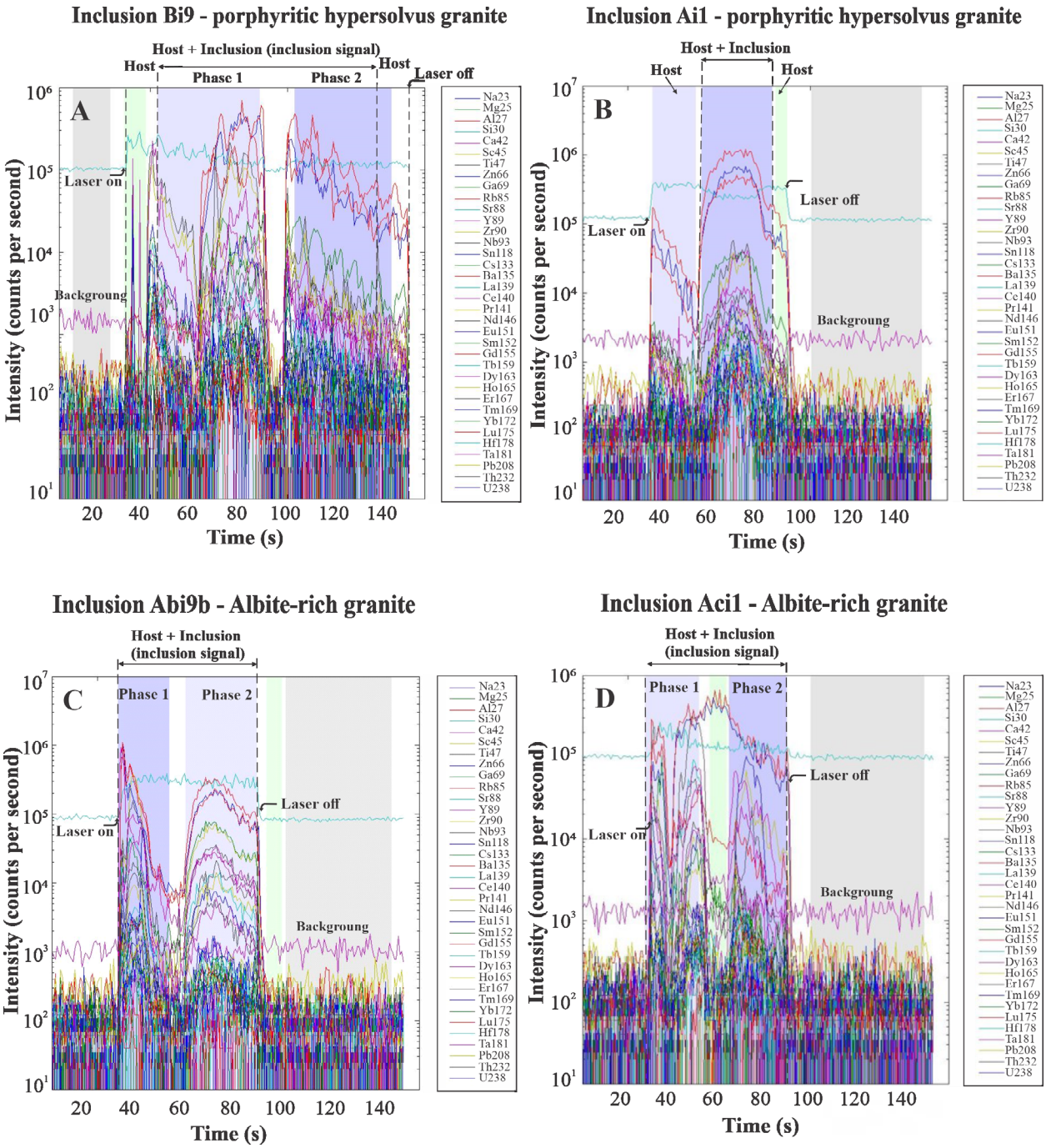

Figure 11. Typical transients signals for thirty-six elements obtained during the ablation of unexposed rehomogeneized silicate melt inclusions in quartz. (A) inclusion Bi9 (see Fig. 9F) and (B) inclusion Ai1 (see Fig. 9C), both in quartz from porphyritic granite (PHR179); (C) inclusion Abi9b (see Fig. 10E) and (D) inclusion Aci1 (see Fig. 10A), both from albite-rich granite (PHR82a). The intervals demarcated in the diagrams represent (I) the signal of the background (blank), (II) the sign of the host only, (III) a mixed signal resulting from the joint ablation of the host and inclusion, and (IV) the signal of the host below inclusion. After ablation of the entire inclusion, the analysis was stopped.

Furthermore, despite the probable loss of important chemical components of the inclusions during the heating experiments (e.g., leakage), the concentrations of elements obtained from LA-ICP-MS analyses (Fig. 12) plot in fields close to the compositions of the respective whole rock (*cf.* Costi 2000).

Analyses of melt inclusions by electron microprobe

Analyses of major elements by electron microprobe were performed both in the glass and globules phases within the melt inclusions of quartz crystals from albite-rich granite and porphyritic granite. The results showed that the globules are compositionally very distinct from the glass phase in porphyritic granite inclusions, being extremely poor in SiO_2 and K_2O, but rich in Na_2O and F (Tab. 3) compared to the glass phase. In the inclusions of albite-rich granite, some globules tend to be relatively poorer in SiO_2 and Al_2O_3, and richer in FeOtot compared to the glass phase.

The concentrations of Na_2O and F, and the index A/CNK demonstrate that the inclusions of both granitic facies evolve in two distinct ways after phase separation, as will be discussed below (Fig. 13).

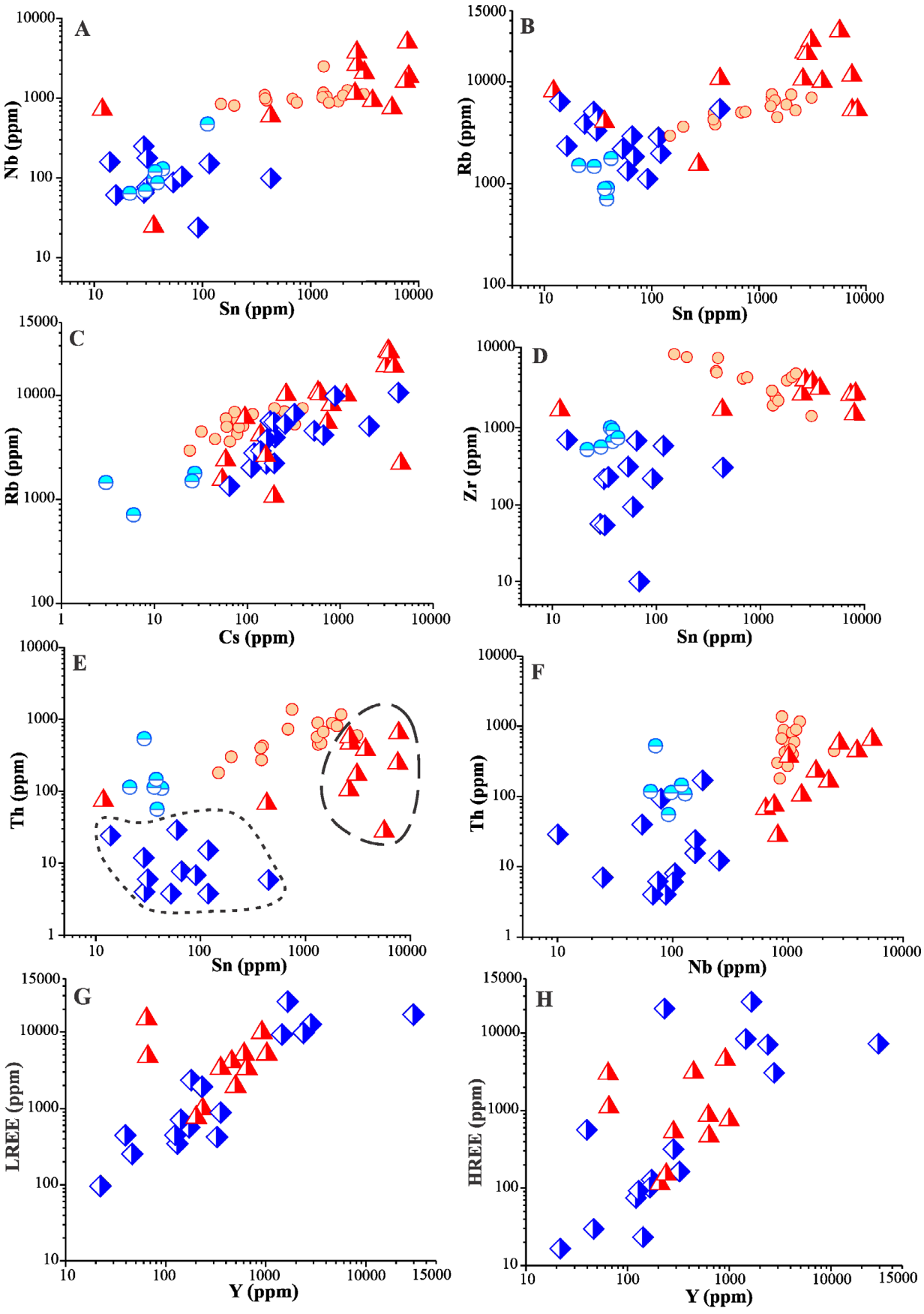

Figure 12. Log-log variation diagrams of (A) Nb vs. Sn; (B) Rb vs. Sn; (C) Rb vs. Cs; (D) Zr vs. Sn; (E) Th vs. Sn; (F) Th vs. Nb; (G) LREE vs. Y, and (H) HREE vs. Y for melt inclusions. LREE (La^{139} + Ce^{140} + Pr^{141} + Nd^{146} + Eu^{151} + Sm^{152} + Gd^{155}); HREE (Tb^{159} + Dy^{163} + Ho^{165} + Er^{167} + Tm^{169} + Yb^{172} + Lu^{175}). Bulk rock data are from Costi (2000) and Costi *et al.* (2009). In diagram (E), the dotted field represents analyzes of magmatic inclusions of porphyritic granite, while the dashed field corresponds to inclusions of albite-rich granite.

Table 3. Major elements composition of quartz melt inclusions from albite-rich granite and hypersolvus porphyritic alkali feldspar granite.

Sample	ArG3 I1-1gl	ArG5 I1-1gl	ArG5 I1-2gl	ArG5 I1-3gl	ArG5 I1-4gl	ArG5 I1-5gl	ArG5 I2-1gb	ArG5 I2-2gb	ArG5 I2-3gl	ArG5 I3-1gl	ArG5 I3-2gl	ArG5 I3-3gl	ArG7 I1-2gb	ArG11 I1-1gl	ArG11 I1-2gl	ArG11 I1-3gl	ArG11 I1-4gb	ArG15 I1-1gl	ArG15 I1-2gl	ArG15 I1-3gl	ArG15 I1-4gb
SiO_2 wt%	74.05	70.69	65.08	65.65	65.94	67.52	64.04	65.98	63.06	68.96	68.56	66.43	78.07	69.86	69.83	72.94	81.84	75.07	70.98	55.47	17.26
Al_2O_3	12.02	13.07	14.07	17.02	17.51	16.59	13.33	11.64	12.36	17.22	17.38	17.89	8.55	11.10	12.15	10.32	4.12	10.82	13.51	15.07	19.09
Na_2O	3.57	4,67	2.92	2.84	2.73	2.75	3.36	2.41	3.36	3.89	3.66	3.94	1.84	3.36	3.64	3.17	1.23	3.14	3.81	5.44	18.48
K_2O	5.1	6.47	8.99	11.38	11.68	11.14	6.72	5.93	6.09	6.69	6.67	6.85	1.63	6.88	7.11	6.39	2.86	4.84	6.17	6.72	2.30
CaO	0.00	0.02	0.08	0.06	0.08	0.02	0.03	0.05	0.04	0.00	0.00	0.00	0.31	0.03	0.00	0.00	0.00	0.12	0.00	0.12	0.85
FeO_{tot}	2.75	1.89	1.99	0.64	0.40	0.54	6.50	6.24	3.61	2.03	1.97	1.97	0.16	3.66	3.23	3.24	1.67	1.35	1.83	2.38	1.07
MgO	0.00	0.00	0.03	0.00	0.00	0.00	0.20	0.22	0.07	0.06	0.04	0.15	0.14	0.00	0.00	0.00	0.00	0.00	0.00	0.02	0.07
MnO	0.12	0.05	0.06	0.01	0.00	0.01	0.19	0.19	0.10	0.07	0.06	0.06	0.01	1.08	0.98	0.99	0.47	0.04	0.04	0.04	0.13
TiO_2	0.33	0.22	0.43	0.13	0.07	0.03	0.71	0.57	0.36	0.04	0.00	0.31	0.03	0.25	0.28	0.29	0.15	0.01	0.05	0.09	0.06
P_2O_5	0.00	0.01	0.01	0.02	0.02	0.01	0.05	0.04	0.02	0.02	0.01	0.02	0.09	0.02	0.00	0.01	0.00	0.00	0.01	0.07	0.34
Cl	0.03	0.01	0.02	0.02	0.01	0.02	0.02	0.03	0.04	0.00	0.01	0.01	0.12	0.01	0.00	0.01	0.01	0.04	0.04	0.04	0.08
F	3.29	2.78	3.67	0.39	0.09	0.11	4.61	4.60	3.35	1.20	1.20	1.37	2.33	3.00	3.23	2.77	0.72	3.74	4.73	16.20	33.48
Total	99.90	98.92	95.90	98.00	98.50	98.70	97.81	96.05	91.28	99.95	99.13	98.53	92.45	98.19	99.13	98.98	92.91	97.63	99.27	95.06	79.20
Sn ppm	190	141	157	0	0	0	299	299	165	299	299	165	78	24	252	165	39	346	401	260	740
A/CNK	1.056	0.887	0.959	0.995	1.014	0.999	1.037	1.114	1.014	1.269	1.313	1.071	1.958	0.854	0.888	0.851	0.806	1.019	1.197	0.917	0.554

Continue...

Table 3. Continuation.

Sample	ArG15 I2-1gl	ArG15 I2-2gl	ArG27 I1-1gl	ArG27 I1-2gl	PG2 I1-1gl	PG2 I1-2gl	PG2 I1-3gl	PG2 I1-4gl	PG13 I1-1gl	PG13 I1-2gl	PG13 I1-3gl	PG14 I1-1gl	PG14 I1-2gl	PG14 I1-3gl	PG14 I1-3gl	PG20 I1-1gl	PG20 I1-2gl	PG20 I1-3gl	PG20 I1-4gb	PG20 I1-1gb
SiO_2 wt%	86.39	67.69	70.56	78.11	72.14	69.95	71.19	73.49	70.71	69.50	72.14	69.03	60,88	59.26	60.08	67.99	66.4	67.35	3.47	3.67
Al_2O_3	5.71	13.12	12.26	7.67	14.18	15,20	14.81	13.24	12.18	12.88	12.61	14.07	14.66	15.10	14.95	13.01	13.42	13.45	19.18	13.87
Na_2O	1.90	3.39	4.09	2.80	1.89	1.81	1.77	1.69	3.98	3.89	4.10	2.84	0.38	0.30	0.31	4.38	5.21	0.01	24.23	16.60
K_2O	3.02	6.30	5.37	3.36	3.94	3.91	3.87	3.91	4.50	4.75	4.64	7.29	10.89	10.83	10.96	5.5	5.77	5.71	0.94	0.93
CaO	0.00	0.00	0.00	0.00	0.00	0.00	0.00	0.00	0.06	0.00	0.00	0.00	0.00	0.00	0.00	0.02	0.06	0.00	1.91	5.50
FeO_{tot}	0.83	1.86	2.00	1.45	1.47	1.48	1.71	2.13	3.02	2.88	3.02	1.81	2.44	3.14	2.61	1.59	1.69	1.69	1.02	1.55
MgO	0.00	0.00	0.00	0.00	0.00	0.00	0.00	0.00	0.00	0.06	0.00	0.00	0.00	0.00	0.00	0.00	0.00	0.00	0.12	0.18
MnO	0.04	0.10	0.01	0.05	0.04	0.03	0.02	0.03	0.09	0.04	0.04	0.02	0.01	0.02	0.01	0.02	0.02	0.01	0.08	0.09
TiO_2	0.06	0.03	0.04	0.02	0.15	0.21	0.21	0.20	0.19	0.19	0.21	0.17	0.22	0.32	0.24	0.13	0.16	0.09	0.30	0.25
P_2O_5	0.01	0.01	0.03	0.01	0.00	0.02	0.01	0.01	0.01	0.01	0.00	0.01	0.02	0.03	0.01	0.01	0.00	0.01	0.04	0.08
Cl	0.01	0.01	0.09	0.26	0.05	0.06	0.05	0.05	0.08	0.12	0.08	0.02	0.01	0.01	0.01	0.02	0.01	0.01	0.08	0.14
F	2.59	5.27	5.29	3.92	5.28	6.08	5.75	5.24	2.73	2.61	2.82	3.78	8.47	8.43	8.64	4.08	6.04	4.44	35.98	39.20
Total	99.54	95.68	97.95	96.05	97.44	96.67	97.52	98.22	96.50	95.88	98.61	97.53	94.41	93.90	94.26	95.18	96.41	91.14	72.35	65.55
Sn ppm	488	921	732	3670	3883	4119	3607	401	433	599	599	0	0	24	0	0	8	0	0	24
A/CNK	0.894	0.978	0.978	0.930	1.909	2.108	2.086	1.855	1.057	1.116	1.072	1.120	1.181	1.236	1.208	0.983	0.889	2.173	0.433	0.364

ArG: albite-rich granite; PG: hypersolvus porphyritic alkali feldspar granite; gl: glass phase; gb: globule phase; I: Melt inclusion; A/CNK: Molar Al_2O_3 / ($CaO + Na_2O + K_2O$); total number of analyses = 41.

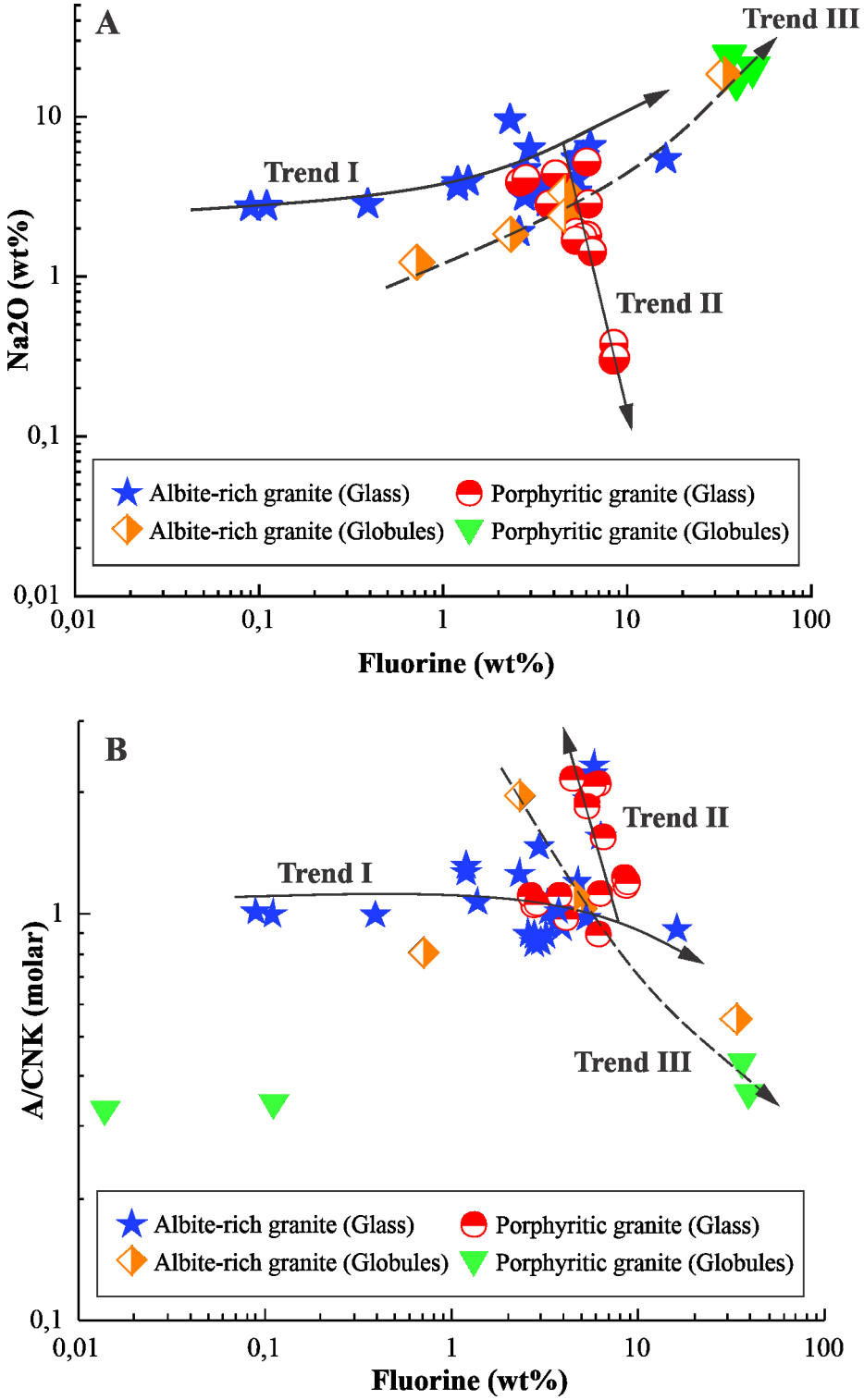

A/CNK: molar ratio of $Al_2O_3/(CaO + Na_2O + K_2O)$.

Figure 13. Distribution of concentrations of fluorine, Na_2O and index A/CNK, obtained from electron microprobe analyses. (A) Na_2O (wt%) x Fluorine (wt%) diagram. (B) A/CNK x Fluorine (wt%) diagram. Trends I, II and III as described in the text.

DISCUSSION

Textures of the magmatic inclusions after quenching and implications for immiscibility

The melt inclusions hosted in quartz phenocrysts of both porphyritic granite and albite-rich granite showed heterogeneous textures after the homogenization and cooling experiments, evidencing a variety of textural types. Despite having different textural features, these inclusion groups coexist at different proportions and in different samples.

The most common textures observed in the melt inclusions from the porphyritic granite are those formed by spherical globules of different sizes, disseminated in a homogeneous glass matrix, with or without a vapor bubble. These heterogeneous textures are called composite textures by Davidson (2004). According to this author, composite inclusions are melt inclusions that have heterogeneously trapped two or more phases

that coexisted in the melt. Typically, they may contain silicate melt (now glass), crystallized silicates, globules of aqueous fluid (liquid or vapor), and microphenocrysts. In the present work, these inclusions are represented by the association of glass with a granular texture, colorless or brown, isolated or clustered globules, and one or more vapor bubbles dispersed in the glass phase.

Some researchers (*cf.* Kamenetsky and Naumov 2003, Davidson 2004) have described these globules as evidence of immiscibility between silicate and salt liquids. Others (Naumov and Kamenestsky 2006) identified salt globules and mentioned several occurrences of salt melts of different compositions, in different geological contexts, and a specific case reports the coexistence of silicate melts and fluoride melts (as salts).

Many inclusions investigated in our study show textures described by Davidson (2004) as bubbly magmatic emulsions, usually formed by the exsolution of aqueous volatile phases from a volatile melt. The magmatic inclusions trapped in quartz crystals of porphyritic granite (Figs. 9A, 9C, and 9F) have textures that are very similar to those described by Davidson (2004), and could probably be representative of a process of exsolution.

The number and size of globules vary significantly, indicating that the silicate glass/globule ratio in the inclusions is highly erratic. According to Roedder (1976), this is strong evidence that immiscibility had occurred before inclusion trapping. In addition, this made it possible for magmatic emulsions to be observed. Magmatic emulsions have also been characterized in melt inclusions in phenocrystic and miarolitic quartz from the tin-bearing Omsukchan granite (NE Russia), in which crystal- and liquid-bearing globules are suspended in a glass "matrix" (Kamenetsky and Naumov 2003).

In the Pitinga samples, it was not possible to analyze the globules separately by LA-ICP-MS. However, the identification of composite textures and the heterogeneous appearance of the phases present in the magmatic inclusions suggest the occurrence of immiscibility, which gave origin to two fractions of melts from a common parental magma.

Unlike porphyritic granite, inclusions trapped in albite-rich granite are mainly of A-type and B-type (Thomas *et al.* 2000). By definition, B-type inclusions are richer in volatile elements and would represent the peralkaline fraction rich in F and H_2O, which has been removed from the precursor magma of porphyritic granite.

Behavior of fluorine during immiscibility between the two granitic melts

Fluorine is a very common element in magmatic and hydrothermal granite systems, and most of the time plays a fundamental role in its evolution.

According to Li *et al.* (2020), high concentrations of fluorine in granitic melts may strongly affect phase stability (e.g., Manning 1981, Veksler *et al.* 2002), melt density and viscosity (e.g., Baasner *et al.* 2013, Bartels *et al.* 2013).

Since fluorine usually behaves as an incompatible element in the processes of magmatic immiscibility (Li *et al.* 2020), in the absence of apatite, mica, amphibole, and fluorite, it would be expected that there would be F enrichment in the separate peralkaline liquid of the parental melt that forms the porphyritic granite.

The occurrence of crystals of REE (bastnäsite-(Ce)), gagarinite-(Y), fluocerite-(Ce) and fluorite, in some crystallized melt inclusions of porphyritic granite (Figs. 6A, 6B, 6C, 6D, and 6E), suggests that the parental melt was already F saturated at the time of the crystallization of these fluorine-bearing phases. The crystallization of these minerals from the silicate melt that originated the porphyritic granite suggests that immiscibility may have occurred early in the coeval evolution of both granites, since these mineral phases are mainly associated with the peralkaline albite-rich granite in Pitinga.

Microprobe data (Tab. 3) allowed us to observe that immiscibility originated two evolutionary paths, designated as trends I and II (Fig. 13A), at the saturation point of the parental magma (4-5% of F?). The Na_2O vs. F diagram shows that the magmatic liquid trapped in the porphyritic granite inclusions had a strong depletion of Na_2O (Fig. 13A; trend II), while the albite-rich granite inclusions showed continuous Na enrichment, together with fluorine, displaying a positive correlation between the two elements (Fig. 13A; trend I). In the A/CNK vs. F diagram, trend II represents the evolution of the porphyritic granite and its increasing peraluminosity, while trend I represents the increasing peralkaline trend of the albite-rich granite.

On the other hand, the globules detected in the inclusions of both albite-rich granite and porphyritic granite showed continuous Na_2O and F enrichment (trend III), following the evolutionary trend of the parental magma. In addition, some globules recorded the most peralkaline compositions of all solid phases analyzed in the melt inclusions (Fig. 13B).

The subsequent F enrichment in the peralkaline liquid forming the albite-rich granite of Pitinga, which has been widely discussed by several authors (Costi 2000, Lenharo *et al.* 2002, 2003, Bastos Neto *et al.* 2009, Costi *et al.* 2009, Bastos Neto *et al.* 2014), is due to its preferential partition, together with H_2O, HFSE, and ore-forming elements, for this specialized granitic liquid.

Enrichment of trace elements in the albite-rich granite

The available chemical data (Tabs. 1 and 2; Fig. 12) indicate that there is strong HFSE (Nb, Ta, Sn, Zr, Th, Y, and REE) enrichment, in addition to some LILE (Rb, Cs) and Sn enrichment, in the melt trapped in the inclusions of the albite-rich granite, compared to that of the porphyritic granite. The elements Nb, Ta, Sn, Y, REE, and Th are important constituents of the rare metal deposits associated with albite-rich granites in the Pitinga mine.

According to Costi *et al.* (2009), the extremely high contents of Zr, Nb, Sn, Hf, Ta, and Th in the albite-rich granite are due to the combination of two factors, the peralkaline composition of the melt and its high concentrations of F, improving the concentration of HFSE during its progressive differentiation.

As reported by Vasyukova and Williams-Jones (2014, 2020), melt inclusions heated to 900–950°C and subjected to quenching generated immiscible fluoride and silicate glasses, suggesting an additional HFSE concentration mechanism in the Strange Lake peralkaline granite pluton. The authors postulate that phase separation (immiscibility), resulting from

the cooling of the heated and homogenized melt inclusions, is strong evidence of immiscibility between the two magmas.

The nucleation of spherical globules during quenching of homogenized inclusions, mainly in the porphyritic granite, but also in the albite-rich granite, is a geological mechanism very similar to that described in Strange Lake pluton. We, therefore, consider this process to be a strong piece of evidence of phase separation, in which a peralkaline liquid may have originated from a precursor magma with geochemical characteristics of the porphyritic granite.

In addition, the textural characteristics and irregular distribution of these globules in the inclusions (variable glass/globules ratio) show that the entrapment of granitic magmas was heterogeneous, and this strongly suggests that liquid immiscibility occurred before their trapping in the quartz host crystals (*cf.* Roedder 1976).

This suggests that globules are formed as a result of an immiscibility process between phases with different physical and chemical properties and that the enrichment of incompatible elements (linear trends in the diagrams on Fig. 12) occurred mainly in the melt inclusions trapped in albite-rich granite quartz.

This enrichment would be associated with a preferential partition process, in which the trace elements would tend to fractionate into the peralkaline fraction, as a result of the greater degree of incompatibility between each of these elements in the melts of this composition (Mahood and Stimac 1990 *apud* Taylor *et al.* 1997). Another important aspect is that, as the quartz phenocrysts that host melt inclusions have no affinity for these trace elements, as they are not incorporated into their structure during magmatic crystallization, the contents of these analyzed elements are extremely faithful at the time of their incorporation into the inclusions.

One of the most important aspects from the metallogenic point of view is that melt inclusions trapped in albite-rich granite quartz crystals are compositionally richer in ore-forming components, such as Sn, Nb, Ta, F, Th, REE, Rb, and Zr. In the case of the Pitinga mine, these elements that preferentially partitioned into the peralkaline fraction formed the rare-metal deposit of the Sn-F-Nb-REE-Zr type, associated with the albite-rich granite.

Melt-melt immiscibility and the probable origin of a peralkaline liquid

Several researchers have discussed the role of liquid immiscibility as an inducer of trace elements and ore-forming elements enrichment, especially in magmas of granite-pegmatite composition (Veksler 2004, Thomas *et al.* 2000, Thomas *et al.* 2003, Rickers *et al.* 2006, Thomas *et al.* 2006a, 2006b, Thomas and Davidson 2013).

Thomas *et al.* (2006) described that the fractional crystallization of an F- and H_2O-rich peraluminous granitic magma improves the melt progressively with volatiles. They show that, at the saturation stage, the melt can separate into two fractions of combined melt, with one of the fractions showing increased peraluminosity and the other increased peralkalinity. These melt fractions also fractionate incompatible elements to significantly different degrees.

In Pitinga, even without studies on melt inclusions, Costi *et al.* (2009) assumed that the peralkaline melt that produced the core albite-rich granite would have originated from a phase separation process (immiscibility), similar to that recorded by Thomas *et al.* (2006) in the Erzgebirge granites. Thus, the peralkaline phase separated from a parental magma which very likely had a slightly peralkaline to metaluminous composition, and with a composition similar to that of the porphyritic granite.

Starting from the premise that the albite-rich granite, with its strong peralkaline signature (Costi 2000), may have been formed by an immiscibility process from a granitic melt already specialized in Na and F, it is very likely that the two granites had a common magmatic source.

The occurrence of silicate globules, mainly in porphyritic granite quartz phenocrysts and, more locally, in the albite-rich granite, is a strong piece of textural evidence of the phase separation process, also suggesting that the immiscibility mechanism probably occurred at an early stage of porphyritic granite evolution, and continued in a more advanced stage, when it reached saturation at least of F and H_2O.

According to Veksler (2004), in volatile-rich magmatic systems, liquid immiscibility is enhanced in peralkaline compositions and in the presence of non-silicate anions such as F^-, Cl^-, CO_3^{2-} and BO_3^{3-}. Based on the mineralogical study carried out in crystallized mineral phases in the inclusions of porphyritic granite (see "Composition of mineral phases in crystallized melt inclusions"), we concluded that the magma that originated this granite already had considerable concentrations of F and CO_2 when it was trapped. Subsequently, with increasing specialization, this felsic melt may have reached a high degree of saturation and triggered the separation of a peralkaline fraction enriched with fluxing elements, HFSE (including REE), and metals that would later give rise to the polymetallic rare-metal deposit (Sn, Nb, Ta, Y, REE, Th, F) associated with the Madeira albite-rich granite.

Therefore, we consider that the data obtained through the study of melt inclusions, including its geochemical signature (major and trace elements), support the hypothesis that a process of melt-melt immiscibility has occurred during the evolution of a parental magma, providing the exsolution of a peralkaline liquid precursor to albite-rich granite.

CONCLUSIONS

This work presents preliminary data from studies of melt inclusions hosted in quartz phenocrysts of the porphyritic hypersolvus alkali feldspar granite and the albite-rich granite, both late facies of the Madeira pluton.

The study identified three populations of magmatic inclusions trapped in quartz crystals: *A-type* and *B-type* inclusions, differentiated by the volume of volatile components (H_2O, F, etc.) immersed in silicate glass (higher volatile volume in B-type), and *composite inclusions*, in which silicate globules of different sizes and abundance occur dispersed in the glass formed during the quenching experiments.

Composite inclusions are melt inclusions that have heterogeneously trapped two or more phases that coexisted in the melt. Some researchers describe them as "magmatic emulsions".

Composite inclusions are prevalent in porphyritic granites, in addition to small amounts of A-type and B-type inclusions. Albite-rich granites contain mainly B-type inclusions, besides some A-type and composite inclusions.

The spherical globules of porphyritic granite composite inclusions represent phases that have been exsolved from a parental silicate melt. We consider that these features are strong evidence of a phase separation process (immiscibility), which triggered the formation of a peralkaline phase precursor of albite-rich granite. The heterogeneous textures of these inclusions are consistent with the hypothesis that liquid immiscibility occurred before melt trapping in the quartz host crystals.

The melt inclusions were initially analyzed by LA-ICP-MS and the chemical data show that the concentrations of trace elements are much higher in albite-rich granite inclusions than in porphyritic granite inclusions, generating chemical enrichment trends between the two granites.

Consequently, melts trapped in albite-granite quartz were richer in Sn, Nb, Ta, Y, Rb, Zr, and Th. Cs has a compositional range that is very similar to that of Rb, and data show that both elements were distributed in a similar manner between the two phases that gave rise to the albite-rich granite and the porphyritic granite.

The rare earth elements (REE) have a distinct geochemical behavior (in albite-rich granites and porphyritic granites). Individually, La and Ce, for example, present their highest concentrations in albite-rich granite inclusions. However, when grouped (LREE and HREE), REE and Y have a strong positive correlation and a very similar compositional variation in both granites.

The occurrence of REE fluorocarbonates (bastnäsite-(Ce)), gagarinite-(Y), fluocerite-(Ce), and fluorite, in some crystallized porphyritic granite melt inclusions, strongly suggests that the parental melt was already F-saturated during the crystallization of these fluorine-bearing phases.

Fluorine and major elements were also analyzed by electron microprobe, in the same melt inclusions analyzed previously by LA-ICP-MS, and the data show that all inclusions displayed expressive fluorine contents. However, after phase separation, the evolutionary trends show F and Na enrichment in albite-rich granites that is relatively greater compared to porphyritic granites.

Although the heating experiments were carried out at atmospheric pressure, the available petrographic data indicate that there was no leakage or decrepitation of the inclusions, even in those inclusions which are richer in volatiles. This means that, very probably, the concentrations of trace elements obtained by chemical analyses were very accurately estimated in view of the composition of the melt at the time of its entrapment in the magmatic inclusions.

This work presents the preliminary results of studies of melt inclusions trapped in rare metal granite minerals, carried out entirely in Brazil, providing an opportunity for future research in magmatic minerals using this methodology.

ACKNOWLEDGEMENTS

The authors thank Mineração Taboca S.A. for providing field work support and access to unpublished data. RMKB is grateful to Coordenação de Aperfeiçoamento de Pessoal de Nível Superior (CAPES) for the post-doctoral fellowship granted. This study is a contribution to Instituto de Geociências da Amazônia — GEOCIAM (INCT–CNPq/MCT/FAPESPA — Process 573733/2008-2). RMKB is very grateful to all CDTN/CNEN staff and fellow researchers who collaborated and made this work possible.

FJR is grateful to CNPq (project 424909/2016-2/), CDTN/CNEN (project 0614.26), FAPEMIG (project PPM00493-15), and FINEP (project REDETEC 2715/09). We appreciate the careful review by Hilton Tulio Costi (MPEG), who has substantially improved this paper. We are also grateful to Gisele Tavares Marques (IG/UFPA) for her support with the electron microprobe analyses.

ARTICLE INFORMATION

Manuscript ID: 20210011. Received on: 02/11/2021. Approved on: 08/24/2021.

R.B. wrote the first draft of the manuscript and prepared all Figures and Tables; L.A. provided support and advice regarding melt inclusions, performed LA-ICP-MS data, and reviewed and improved the manuscript; F.R. supervised the research of the first author, and improved the manuscript through corrections and suggestions; G.S. provided EPM data; M. F. provided support and advice regarding melt inclusions; T.L. provided laboratory support; A.S. provided laboratory support and T.P. provided SEM/EDS data.

Competing interests: the authors declare no competing interests.

REFERENCES

Agangi A., Hofmann A., Kamenetsky V.S., Vroon P.Z. 2015. Paleoarchean felsic magmatism: a melt inclusion study of 3.45 Ga old rhyolites from the Barberton Greenstone Belt, South Africa. *Chemical Geology*, **414**:69-83. https://doi.org/10.1016/j.chemgeo.2015.09.002

Allan M.M., Yardley B.W.D., Forbes L.J., Shmulovich K.I., Banks, D.A., Shepperd T.J. 2005. Validation of LA–ICP–MS fluid inclusion analysis with synthetic fluid inclusions. *American Mineralogist*, **90**:1767-1775. https://doi.org/10.2138/am.2005.1822

Almeida F.F.M., Hasui Y., Brito Neves B.B., Fuck R.A. 1981. Brazilian Structural Provinces: an introduction. *Earth-Science Review*, **17**(1-2):1-29. https://doi.org/10.1016/0012-8252(81)90003-9

Almeida M.E. 2006. *Evolução geológica da porção centro-sul do Escudo das Guianas com base no estudo geoquímico, geocronológico e isotópico dos granitoides Paleoproterozoicos do Sudeste de Roraima, Brasil*. PhD Thesis, Universidade Federal do Pará, Belém, 227 p.

Amorim L.E.D., Freitas M.E., Rios F.J., Lima T.A.F. 2012. Melt inclusions: Principais características e técnicas de estudo. *Geonomos*, **20**(2):58-67. https://doi.org/10.18285/geonomos.v2i20.248

Araújo Neto H., Moreira H.L. 1976. *Projeto Abonari–Relatório Final*. Manaus: Departamento Nacional da Produção Mineral/Companhia de Pesquisa de Recursos Minerais.

Baasner A., Schmidt B., Webb S.L., 2013. The effect of chlorine, fluorine and water on the viscosity of aluminosilicate melts. *Chemical Geology*, **357**:134-149. https://doi.org/10.1016/j.chemgeo.2013.08.020

Bartels A., Behrens H., Holtz F., Schmidt B.C., Fechtelkord M., Knipping J., Crede L., Baasner A., Pukallus N. 2013. The effect of fluorine, boron and phosphorus on the viscosity of pegmatite forming melts. *Chemical Geology*, **346**:184-198. https://doi.org/10.1016/j.chemgeo.2012.09.024

Bastos Neto A.C., Ferron J.M.T.M., Chauvet A., Chemale Jr. F., Lima E.F., Barbanson L., Costa C.F.M. 2014. U-Pb dating of the Madeira Suite and structural control of the albite-enriched granite at Pitinga (Amazonia, Brazil): Evolution of the A- type magmatism and implications for the genesis of the Madeira Sn-Ta-Nb (REE, cryolite) world-class deposit. *Precambrian Research*, **243**:181-196. https://doi.org/10.1016/j.precamres.2013.12.021

Bastos Neto A.C., Pereira V.P., Lima E.F., Ferron J.M., Minuzzi O., Ronchi L.H., Flores J.A.A., Frantz J.C., Pires A.C., Pierosan R., Hoff R., Botelho N.F., Rolim S.B.A., Rocha F.N.F., Ulmann L. 2005. A jazida de criolita da mina Pitinga (Amazonas). *In*: Marini J.O., Queiroz E., Ramos B.W. (Eds.) *Caracterização de depósitos minerais em distritos mineiros da Amazônia*. Brasília: DNPM–ADIMB, p. 477-552.

Bastos Neto A.C., Pereira V.P., Ronchi L.H., Lima E.F., Frantz J.C. 2009. The world-class Sn, Nb, Ta, F (Y, REE, Li) deposit and the massive cryolite associated with the albite enriched facies of the Madeira A-type granite, Pitinga mining district, Amazonas state, Brazil. *The Canadian Mineralogist*, **47**(6):1329-1357. https://doi.org/10.3749/canmin.47.6.1329

Bodnar R.J., Student J.J. 2006. Melt *Inclusions in plutonic rocks:* Petrography and Microthermometry. Short Course Series, Mineralogical Association of Canada, **36**:1-25.

Costi H.T. 2000. *Petrologia de granitos alcalinos com alto F mineralizados em metais raros: O exemplo do albita-granito da mina Pitinga, Amazonas, Brasil.* PhD Thesis, Universidade Federal do Pará, Belém, 361 p.

Costi H.T., Borges R.M.K., Dall'Agnol R.D. 2005. Depósitos de estanho da mina Pitinga, Estado do Amazonas. *In*: Marini J.O., Queiroz E., Ramos B.W. (Eds.). *Caracterização de depósitos minerais em distritos mineiros da Amazônia*. Brasília: DNPM–ADIMB, p. 391-475.

Costi H.T., Dall'Agnol R., Moura C.A.V. 2000. Geology and Pb–Pb geochronology of Paleoproterozoic volcanic and granitic rocks of the Pitinga Province, Amazonian craton, northern Brazil. *International Geology Review*, **42**(9):832-849. https://doi.org/10.1080/00206810009465114

Costi H.T., Dall'Agnol R., Pichavant M., Rämö O.T. 2009. The peralkaline tin-mineralized Madeira cryolite albite-rich granite of Pitinga, Amazonian craton, Brazil: Petrography, mineralogy and crystallization processes. *The Canadian Mineralogist*, **47**(6):1301-1327. https://doi.org/10.3749/canmin.47.6.1301

Danyushevsky L.V., McNeill A.W., Sobolev A.V. 2002. Experimental and petrological studies of melt inclusions in phenocrysts from mantle-derived magmas: an overview of techniques, advantages and complications. *Chemical Geology*, **183**(1-4):5-24. https://doi.org/10.1016/S0009-2541(01)00369-2

Davidson P. 2004. *A new methodology for the study of the magmatic–hydrothermal transition in felsic magmas: applications to barren and mineralized systems*. PhD Thesis, University of Tasmania, Hobart, Australia, 274 p.

Davidson P., Kamenetsky V.S. 2001. Immiscibility and continuous felsic melt-fluid evolution within the Rio Blanco porphyry system, Chile: evidence from inclusions in magmatic quartz. *Economic Geology*, **96**(8):1921-1929. https://doi.org/10.2113/gsecongeo.96.8.1921

Dietrich A., Lehmann B., Wallianos A. 2000. Bulk rock and melt inclusion geochemistry of Bolivian tin porphyry systems. *Economic Geology*, **95**(2):313-326. https://doi.org/10.2113/gsecongeo.95.2.313

Ferron J.M.T.M., Bastos Neto A.C., Lima E.F., Costi H.T., Moura C.A.V., Prado M., Pioresan R., Galarza M.A. 2006. Geology and Pb–Pb geochronology of granitic and volcanic acid to intermediate Paleoproterozoic rocks from the Pitinga province, Amazonian craton. *Revista Brasileira de Geociências*, **36**(3):499-512. http://dx.doi.org/10.25249/0375-7536.2006363499512

Frezzotti M.L. 2001. Silicate-melt inclusions in magmatic rocks: application to petrology. *Lithos*, **55**(1-4):273-299. https://doi.org/10.1016/S0024-4937(00)00048-7

Gibbs A.K., Barron C.N. 1983. The Guiana Shield reviewed. *Episodes*, **6**(2):7-14. https://doi.org/10.18814/epiiugs/1983/v6i2/003

Guillong M., Meier D.L., Allan M., Heinrich C.A., Yardley B.W.D. 2008. *Sills:* a MATLAB-based program for the reduction of laser ablation ICP-MS data of homogeneous materials and inclusion. Short Course 4. Vancouver, B.C.: Mineralogical Association of Canada, p. 328-3330.

Halter W.E., Pettke T., Heinrich C.A. 2004. Laser-ablation ICP-MS analysis of silicate and sulfide melt inclusions in an andesitic complex I: analytical approach and data evaluation. *Contribution to Mineralogy and Petrology*, **147**:385-396. https://doi.org/10.1007/s00410-004-0562-6

Halter W.E., Pettke T., Heinrich C.A., Rothen-Rutishauser B. 2002. Major to trace element analysis of melt inclusions by laser ablation ICP-MS: methods of quantification. *Chemical Geology*, **183**(1-4):63-86. https://doi.org/10.1016/S0009-2541(01)00372-2

Hansteen T. 1991. Multi-stage evolution of the picritic Maelifell rocks, SW Iceland: constraints from mineralogy and inclusions of glass and fluid in olivine. *Contributions to Mineralogy and Petrology*, **109**:225-239. https://doi.org/10.1007/BF00306481

Kamenetsky V.S. 2006. *Melt inclusion record of magmatic immiscibility in crustal and mantle magmas*. Short Course 36. Vancouver, B.C.: Mineralogical Association of Canada, p. 81-98.

Kamenetsky V.S., De Vivo B., Naumov V.B., Kamenestky M.B., Menagh T.P., Achterbergh E.V., Ryan C.G., Davidson P. 2003. Magmatic inclusions in the search for natural silicate-salt melt immiscibility: Methodology and examples. *Developments in Volcanology*, **5**:65-82. https://doi.org/10.1016/S1871-644X(03)80024-4

Kamenetsky V.S., Kamenetsky M.B. 2010. Magmatic fluids immiscible with silicate melts: Examples from inclusions in phenocrysts and glasses, and implications for magma evolution and metal transport. *Geofluids*, **10**:293-311. https://doi.org/10.1111/j.1468-8123.2009.00272.x

Kamenetsky V.S., Naumov V.B. 2003. Melt inclusion evidence for immiscibility between silicate and salt liquids in a common granite magma. *Acta Mineralogica-Petrographica*, Abstract Series 2, Szeged, p. 97-98.

Lenharo S.L.R., Moura M.A., Botelho N.F. 2002. Petrogenetic and mineralization processes in Paleo- to Mesoproterozoic rapakivi granites: examples from Pitinga and Goiás, Brazil. *Precambrian Research*, **119**(1-4):277-299. https://doi.org/10.1016/S0301-9268(02)00126-2

Lenharo S.L.R., Pollard P.J., Born H. 2003. Petrology and textural evolution of granites associated with tin and rare-metals mineralization at the Pitinga mine, Amazonas, Brazil. *Lithos*, **66**(1-2):37-61. https://doi.org/10.1016/S0024-4937(02)00201-3

Li X., Zhang, C., Wang L., Behrens H., Holtz, F. 2020. Experiments on the saturation of fluorite in magmatic systems: implications for maximum F concentration and fluorine-cation bonding, in silicate melt. *Journal of Earth Science*, **31**(3):456-467. https://doi.org/10.1007/s12583-020-1305-y

Lowenstern J.B. 1995. Applications of silicate-melt inclusions to the study of magmatic volatiles. *In*: Thompson J.F.H. (Ed.). *Magmas, fluids, and ore deposits*. MAC Short Course, v. 23, Victoria, British Columbia: Mineralogy Association of Canada, p. 71-100.

Lukkari S., Thomas R., Haapala I. 2009. Crystallization on the Kymi topaz granite stock within the Wiborg rapakivi granite batholith, Finland: Evidence from melt inclusions. *The Canadian Mineralogist*, **47**(6):1359-1374. https://doi.org/10.3749/canmin.47.6.1359

Manning D.A.C. 1981. The effect of fluorine on liquidus phase relationships in the system Qz-Ab-Or with excess water at 1 kb. *Contributions to Mineralogy and Petrology*, **76**(2):206-215. https://doi.org/10.1007/bf00371960

Minuzzi O.R.R. 2005. *Gênese e evolução da mineralização de criolita, pirocloro e columbita da subfácies albita granito de núcleo, Mina Pitinga, Amazonas, Brasil*. PhD Thesis, Universidade Federal do Rio Grande do Sul, Porto Alegre, Brasil, 249 p.

Naumov V.B., Kamenestsky V.S. 2006. Silicate and salt melts in the genesis of the industrial'noe tin deposit: evidence from inclusions in minerals. *Geochemistry International*, **44**(12):1181-1190. https://doi.org/10.1134/S0016702906120032

Pettke T. 2006. In situ laser ablation-ICP-MS chemical analysis of melt inclusions and prospects for constraining subduction zone magmatism. *In*: Webster J.D. (ed.). *Melt inclusions in plutonic rocks*. Mineralogical Association Canada Short Course, **36**:51-80.

Pires A.C. 2010. *Xenotima, gagarinita, fluocerita e waimirita da Mina Pitinga (AM): Mineralogia e avaliação preliminar do potencial do albita granito para exploração de elementos terras raras e ítrio*. PhD Thesis, Universidade Federal do Rio Grande do Sul, Porto Alegre, Brasil, 199 p.

Rickers K., Thomas R., Heinrich W. 2006. The behavior of trace elements during the chemical evolution of the H_2O-, B-, and F-rich granite–pegmatite-hydrothermal system at Ehrenfriedersdorf, Germany: a SXRF study of melt and fluid inclusions. *Mineralium Deposita*, **41**(3):229-245. https://doi.org/10.1007/s00126-006-0057-7

Roedder E. 1976. Petrologic data from experimental studies on crystallized melt and other inclusions in lunar and Hawaiian olivine. *American Mineralogist*, **61**(7-8):684-690.

Roedder E. 1979. Origin and significance of magmatic inclusions. *Bulletin de Minéralogie*, **102**:487-510. https://doi.org/10.3406/bulmi.1979.7299

Roedder E. 1984a. Fluid inclusions. *Reviews in Mineralogy*, **12**:1-644.

Roedder E. 1984b. Occurrence and significance of magmatic inclusions and silicate liquid immiscibility. *Acta Geologica Polonica*, **34**(1-2):139-178.

Santos J.O.S., Hartmann L.A., Faria M.S.G. de, Riker S.R.L., Souza M.M. de, Almeida M.E., McNaughton N.J. 2006. A compartimentação do Cráton Amazonas em províncias: avanços ocorridos no período 2000-2006. *In*: Simpósio de Geologia da Amazônia, 9, Belém. SBG-Núcleo Norte. CD-ROM.

Santos J.O.S., Hartmann L.A., McNaughton N.J., Fletcher I.R. 2002. Timing of mafic magmatism in the Tapajos Province (Brazil) and implications for the evolution of the Amazon craton: evidence from baddeleyite and zircon U-Pb SHRIMP geochronology. *Journal of South America Earth Science*, **15**(4):409-429. https://doi.org/10.1016/S0895-9811(02)00061-5

Skirius C.M., Peterson J.W., Anderson Jr. A.T. 1990. Homogenizing rhyolitic glass inclusions from Bishop Tuff. *American Mineralogist*, **75**(11-12):1381-1398.

Sorby H.C. 1858. On the microscopic structure of crystals, indicating the origin of minerals and rocks. *Quarterly Journal of the Geological Society*, **14**:453-500. https://doi.org/10.1144/GSL.JGS.1858.014.01-02.44

Student J.J., Bodnar R.J. 1996. Melt inclusion microthermometry: petrologic constraints from the H_2O-saturated haplogranite system. *Petrology*, **4**(3):291-306.

Student J.J., Bodnar R.J. 1999. Synthetic fluid inclusions XIV: microthermometric and compositional analysis of coexisting silicate melt and aqueous fluid inclusions trapped in the haplogranite–H_2O–NaCl–KCl system at 800°C and 2000 bars. *Journal of Petrology*, **40**(10):1509-1525. https://doi.org/10.1093/petroj/40.10.1509

Student J.J., Bodnar R.J. 2004. Silicate melt inclusions in porphyry copper deposits: Identification and homogenization behavior. *Canadian Mineralogist*, **42**(5):1583-1599. https://doi.org/10.2113/gscanmin.42.5.1583

Taylor R.P., Jackson S.E., Longerich H.P., Webster J.D. 1997. In situ trace-element analysis of individual silicate melt inclusions by laser ablation microprobe-inductively coupled plasma-mass spectrometry (LAM-ICP-MS). *Geochimica et Cosmochimica Acta*, **61**(13):2559-2567. https://doi.org/10.1016/S0016-7037(97)00109-9

Thomas R. 2000. Determination of water contents of granite melt inclusions by confocal laser Raman microprobe spectroscopy. *American Mineralogist*, **85**(5-6):868-872. https://doi.org/10.2138/am-2000-5-631

Thomas R., Davidson P. 2013. The missing link between granites and granitic pegmatites. *Journal of Geosciences*, **58**(2):183-200.

Thomas R., Davidson P., Beurlen H. 2012. The competing models for the origin and internal evolution of granitic pegmatites in the light of melt and fluid inclusion research. *Mineralogy and Petrology*, **106**:55-73. https://doi.org/10.1007/s00710-012-0212-z

Thomas R., Förster H.-J., Heinrich W. 2003. The behavior of boron in a peraluminous granite-pegmatite system and associated hydrothermal solutions: a melt and fluid-inclusion study. *Contribution to Mineralogy and Petrology*, **144**:457-472. https://doi.org/10.1007/s00410-002-0410-5

Thomas R., Klemm W. 1997. Microthermometric study of silicate melt inclusions in variscan granites from SE Germany: volatile contents and entrapment conditions. *Journal of Petrology*, **38**(12):1753-1765. https://doi.org/10.1093/petroj/38.12.1753

Thomas R., Webster J.D., Heinrich W. 2000. Melt inclusions in pegmatite quartz: complete miscibility between silicate melts and hydrous fluids at low pressure. *Contribution to Mineralogy and Petrology*, **139**:394-401. https://doi.org/10.1007/s004100000120

Thomas R., Webster J.D., Rhede D., Seifert W., Rickers K., Förster H.-J., Heinrich W., Davidson P. 2006. The transition from peraluminous to peralkaline granitic melts: evidence from melt inclusions and accessory minerals. *Lithos*, **91**(1-4):137-149. https://doi.org/10.1016/j.lithos.2006.03.013

Vasyukova O., Williams-Jones A.E. 2014. Fluoride–silicate melt immiscibility and its role in REE ore formation: evidence from the Strange Lake rare metal deposit, Québec-Labrador, Canada. *Geochimica et Cosmochimica Acta*, **139**:110-130. https://doi.org/10.1016/j.gca.2014.04.031

Vasyukova O., Williams-Jones A.E. 2020. Partial melting, fractional crystallization, liquid immiscibility and hydrothermal mobilization – a 'recipe' for the formation of economic A-type granite-hosted HFSE deposits. *Lithos*, **356-357**:105300. https://doi.org/10.1016/j.lithos.2019.105300

Veiga Jr. J.P., Nunes A.C.B., Fernandes A.S., Amaral J.A.F., Amaral J.E., Pessoa M.R., Cruz S.A.S. 1979. *Projeto Sulfetos de Uatumã*. Manaus: Departamento Nacional da Produção Mineral – Companhia de Pesquisa de Recursos Minerais (DNPM/CPRM). 7 v.

Veksler I.V. 2004. Liquid immiscibility and its role at the magmatic–hydrothermal transition: a summary of experimental studies. *Chemical Geology*, **210**(1-4):7-3. https://doi.org/10.1016/j.chemgeo.2004.06.002

Veksler I.V., Thomas R., Schmidt C. 2002. Experimental evidence of three coexisting immiscible fluids in synthetic granitic pegmatite. *American Mineralogist*, **87**(5-6):775-779. https://doi.org/10.2138/am-2002-5-621